JOURNAL OF GUIDANCE, CONTROL, AND DYNAMICS
Vol. 49, No. 2, February 2026

Application of Fundamental Modal Solutions to Relative Dynamics in the Cislunar Environment

Claudio Vela,* Roberto Opromolla,† and Giancarmine Fasano‡
University of Naples Federico II, 80125 Naples, Italy
and
Hanspeter Schaub§
University of Colorado Boulder, Boulder, Colorado 80309

https://doi.org/10.2514/1.G009347

The rising interest in cislunar space as a strategic environment for easier access to the Moon and the solar system has fostered the development of several future missions. In such an environment, close-proximity operations will require innovative trajectory design and path-planning techniques. Moving toward this goal, this paper introduces an original relative motion representation with respect to a periodic chief in the circular restricted three-body problem and an original relative trajectories design methodology based on fundamental modal solutions decomposition. Specifically, a relative motion model is developed in a velocity-based orbiting frame, in which the flight-path direction is considered to define one of its primary axes. Then, modal decomposition is applied to separate the fundamental modes of motion, showing that modal coefficients, eigenvectors, and eigenvalues can be employed for a geometrical characterization of relative dynamics. The resulting relative motion model is applied to describe the relative dynamics between a chaser spacecraft and a target satellite moving onto an L2 halo orbit, and its accuracy is assessed by comparisons against numerical integration of the three-body problem equations. In addition, the use of modal decomposition coefficients as geometrically insightful relative orbital elements for trajectory design and path planning is illustrated through various applicative examples.

I. Introduction

THE importance of close-proximity operations (CPOs) in the current space environment has increased over the years. In the near-Earth space, methodologies for CPOs are being investigated to deal with the current satellite overpopulation by enabling a wide range of on-orbit services [1,2]; in the cislunar space, a similar trend is manifesting [3–8], also in view of the prospective use of this environment as a bridgehead for Moon and solar system exploration [9,10]. In this respect, many studies have investigated the feasibility of CPOs in cislunar space [11–15], showing that a deeper understanding of the dynamics of the problem is necessary and can be achieved through the development of relative motion models with different levels of complexity.

Upon first approaching the problem of CPOs in cislunar space, models with a simple mathematical formulation are preferred for mission analysis and design and are often derived within the framework of the circular restricted three-body problem (CR3BP). In the CR3BP, the two primary centers of gravity (in this case, the Earth and Moon) are assumed to revolve in a circular motion (circularization assumption) and the mass of a third body such as a spacecraft is considered negligible (restriction assumption). Under these assumptions, five equilibrium points known as Lagrange points (usually labeled L1 to L5) can be identified; motions occurring in the proximity of these points can be described analytically [16] or through a linearization of the equations of motion [17]. For these reasons, the CR3BP is often employed as a valuable starting point before more complicated representations are introduced. In fact, high-accuracy models are preferred for onboard guidance, navigation, and control (GNC) tasks because the eccentricity of the orbit of the Moon around the Earth and the effects of the main perturbing forces acting in the cislunar space (such as solar radiation pressure and the gravitational pull of the sun) cannot be neglected during GNC operations [18]. In their work, Colombi, Colagrossi, and Lavagna [19] relied on CR3BP dynamics for mission design purposes and later expanded their model for spacecraft control by including planetary ephemerides to consider the gravitational effects of other celestial bodies, solar radiation pressure, and orbit–attitude coupling. Similarly, Franzini and Innocenti [20] developed sets of nonlinear and linearized differential equations to describe relative dynamics in the restricted three-body problem (R3BP) and subsequently expanded the formulation to a four-body problem by introducing the gravitational perturbation of the sun, further including the effect of solar radiation pressure. A CR3BP formulation of relative dynamics was employed by Scorsoglio et al. [21] to solve guidance problems with the zero-effort-miss/zero-effort-velocity formulation.

Together with an appropriate modeling of relative dynamics, finding an effective way to represent them can substantially ease trajectory design and planning by providing geometrical insight and allowing the exploitation of natural dynamics. In this respect, Segerman et al. [16] represented their analytical solutions in terms of the amplitude and phase of motion along each Cartesian component so that these quantities can be used for trajectory design. Likewise, Elliot and Bosanac [22] derived a set of relative motion equations in a local-vertical/local-horizon frame involving geometrical parameters for the description of quasi-periodic motions around the target. A different perspective on relative motion design was achieved through the analysis of the eigenvalues and eigenvectors of the state transition matrix (STM) of the motion. In this spirit, Zuehlke et al. [23] and Zuehlke et al. [24] exploited an exponential matrix model for relative motion description in the CR3BP to find natural periodic solutions through a single-shooting differential correction method. Bucci et al. [25] used the

Presented as Paper 2025-2601 at the 2025 AIAA SciTech Forum and Exposition, Hyatt Regency Orlando, Orlando, FL, 6–10 January 2025; received 16 May 2025; accepted for publication 7 November 2025; published online 31 December 2025.

*Postdoctoral Research Fellow, Department of Industrial Engineering; claudio.vela@unina.it Young Professional Member AIAA (Corresponding Author).

†Assistant Professor, Department of Industrial Engineering; roberto.opromolla@unina.it Member AIAA.

‡Full Professor, Department of Industrial Engineering; giancarmine.fasano@unina.it AIAA Senior Member.

§Professor and Department Chair, Schaden Leadership Chair, Ann and H.J. Smead Department of Aerospace Engineering Sciences, Colorado Center for Astrodynamics Research; hanspeter.schaub@colorado.edu. Fellow AIAA.

spectral analysis of the STM to identify stable and unstable manifolds, and they used them for mission design and guidance purposes; a similar approach was considered by Colombi et al. [19] and by Bucchioni and Innocenti [12]. The analysis of the eigenvectors of a periodic orbit in the CR3BP framework allowed Takubo et al. [26] to identify a set of local toroidal coordinates to describe the bounded quasi-periodic relative dynamics of a spacecraft around this orbit.

Within this framework, the introduction of the Lyapunov–Floquet (LF) transformation derived from the Floquet theory for the analysis of periodic systems [27] provides a powerful tool for relative dynamics modeling and control, although its application has been investigated in few research works [28–31]. When applied to a linear time-varying (LTV) system, such as the one representing the linearized dynamics of relative motion in the CR3BP, the LF transformation allows decomposition of the motion into fundamental modes, such as drifting (stable or unstable) and oscillatory contributions. In this way, any solution of the relative motion problem can be expressed as a weighted sum of such fundamental terms, which are functions of the eigenvectors and eigenvalues of the relative dynamics. The coefficients that weigh each mode of motion thus act as constants of integration and can be considered as equivalent to a set of relative orbital elements (ROEs). As such, they carry insightful information on the geometry of the free relative dynamics and can be used as representations of the relative state within path-planning, guidance, and control methodologies. Burnett and Schaub [32–34] focused on the application of this modal decomposition approach to different motion regimes (including the CR3BP) and used the coefficients of modal decomposition as ROEs for impulsive and continuous-time path planning. Bai et al. [35] applied the LF transformation to retrieve the modes of motion representing the relative dynamics around a target spacecraft on an eccentric Earth orbit, and they showed that the initial conditions of the linear time-invariant (LTI) system act as constants of integration of the motion, which can be used for relative motion control purposes. Following previous research efforts, Cuevas del Valle et al. [36] used Floquet's theory to find the eigenvalues and eigenvectors of the modes of motion and then designed a station-keeping control strategy targeting the unstable ones.

In this research context, this paper proposes an original relative motion model and expresses its solutions through decomposition in fundamental modes to gain geometrical insight for trajectory design and path planning. Specifically, first, nonlinear and linearized models for the relative dynamics in a cislunar environment are developed in the CR3BP framework and assume a periodic motion for the target spacecraft. The equations of relative motion are presented in an orbiting target-fixed velocity-based frame, in which one of the axes is aligned with the instantaneous velocity vector of the target. This representation is more intuitive as compared to the one achieved in other orbiting frames because it is closer to what would be observed on an elliptic orbit around the Earth. Second, the method of fundamental modal solutions presented by Burnett and Schaub [33,34] is applied to the proposed linearized model of motion to express the solutions to the equations of motion, and the related coefficients of modal decomposition can be used to geometrically characterize the dynamics. The resulting relationship between the geometrical properties of the motion and the coefficients of modal decomposition is then used to provide examples of trajectory design. Finally, the mathematical relation between control actions applied to the spacecraft and variations in the coefficients of modal decomposition is recalled, and the use of the coefficients as ROEs for guidance tasks is explored.

The paper is structured as follows. First the absolute and relative dynamics are presented in Sec. II, which also addresses the derivation of the equations of relative motion in the velocity-based frame. At this point, the method of fundamental modal solutions decomposition is briefly recalled and the geometrical analysis of each mode of motion is conducted in Sec. III, in which relations are provided to bind the coefficients to the geometrical properties of the motion. The derived methodologies are then applied to specific cases of interest in Sec. IV, including the design of periodic, quasi-periodic, and drifting motions, and the evaluation of the impulsive ΔVs for the execution of an approach maneuver. Finally, conclusions are drawn in Sec. V.

II. Dynamics in the Circular Restricted Three-Body Problem

In this work, the absolute motion of the target spacecraft is assumed to be described by CR3BP equations, in which periodic or quasi-periodic orbits for the target spacecraft can be found. However, this choice does not limit the validity of the proposed methodology, which remains valid regardless of the description of the absolute dynamics of the motion as long as the assumption of a periodic trajectory for the target spacecraft is respected.

Before introducing the equations of motion, the mathematical notation and reference frames considered throughout the paper are presented. Given a generic vectorial physical entity $\boldsymbol{v}$, its norm is represented as v if not differently stated, and notation $[\boldsymbol{v}]_a^b$ is employed to specify that it is observed in frame A but expressed in B. The notation simplifies to $[\boldsymbol{v}]_b$ if A and B are the same frame; it further reduces to $\boldsymbol{v}$ if the physical entity is considered without the need to specify a reference frame. The passive rotation matrix from B to A is represented as R_b^a. Vector $\boldsymbol{\omega}_{ab}$ represents the angular velocity with which A rotates with respect to B, whereas Ω_{ab} is the skew-symmetric matrix equivalent to a cross-product by $\boldsymbol{\omega}_{ab}$ Moreover, the notation $[\boldsymbol{\omega}_{ab}]^a$ and $[\Omega_{ab}]^a$ is employed to specify that the angular velocity vector or matrix is expressed in frame A. The dot notation $(\dot{\circ})$ is used to express differentiation with respect to time; multiple dots imply that differentiation occurs multiple times. Finally, dimensional quantities are represented using the symbol "$\bar{\circ}$"; if not specified, the considered quantity is dimensionless.

Concerning the considered reference frames, first, an inertial reference frame (IRF) is defined as $\{B, \hat{I}, \hat{J}, \hat{K}\}$ and indicated using letter "I". Origin B of the IRF is in the barycenter of the system of the two primary bodies (the Earth and Moon), around which they rotate, whereas the IRF axes are aligned with those of the classical Earth-centered inertial frame. Then, a Moon-centered x/y inverted synodal reference frame (MRF) that rotates together with the Earth–Moon system is defined as $\{M, \hat{x}_{\text{MRF}}, \hat{y}_{\text{MRF}}, \hat{z}_{\text{MRF}}\}$, indicated with the letter "M" and having its origin in the Moon. The x axis of the MRF instantaneously points toward the Earth, the z axis is parallel to the angular velocity of rotation of the Earth–Moon system with respect to the IRF $\boldsymbol{\omega}_{mi}$, and the y axis completes the right-handed frame. The MRF definition, inherited from [20], is preferred to the classical synodal barycentric reference frame because the considered trajectories are closer to the Moon than to Earth. Finally, the orbiting reference frame in which the relative motion equations are developed is defined as a velocity reference frame (VRF) [37], represented as $\{V, \hat{i}, \hat{j}, \hat{k}\}$ and indicated with letter "V". The frame has its origin in the target spacecraft, with the y axis aligned with the instantaneous velocity vector, the z axis aligned with the instantaneous angular momentum vector, and the x axis completing the right-handed frame. Notably, a similar reference frame was also used by Takubo et al. [26] to represent relative dynamics in the CR3BP, although using different axes ordering. A graphical representation of the reference frames discussed so far is provided in Fig. 1.

In this mathematical framework, the vector equation of the R3BP representing the absolute motion of a spacecraft with respect to the Moon can be expressed in dimensional quantities in the IRF as in Eq. (1), where $\boldsymbol{r}$ represents the position vector of the spacecraft, $\boldsymbol{r}_{em}$ is the position vector of the Moon with respect to the Earth, and $\overline{\mu}_e$ and $\overline{\mu}_m$ are the gravitational parameters of the Earth and Moon:

$$[\ddot{\bar{\boldsymbol{r}}}]_i = -\overline{\mu}_m \frac{[\bar{\boldsymbol{r}}]_i}{\bar{r}^3} - \overline{\mu}_e \left(\frac{[\bar{\boldsymbol{r}} + \bar{\boldsymbol{r}}_{em}]_i}{\|\bar{\boldsymbol{r}} + \bar{\boldsymbol{r}}_{em}\|^3} - \frac{[\bar{\boldsymbol{r}}_{em}]_i}{\bar{r}_{em}^3} \right) \tag{1}$$

The R3BP equations are usually reported in their dimensionless form by imposing that 1) the sum of the dimensionless masses of the primaries equals unity; 2) the sum of the dimensionless distances of the primaries from their barycenter equals unity, i.e., $r_{em} = 1$; and

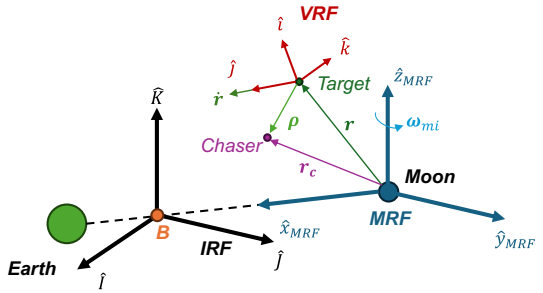

Fig. 1 Graphical representation of the reference frames and their relationship.

3) the time unit of the system is the inverse of the synodal frequency $\overline{\omega}_{mi}$ so that the dimensionless synodal frequency equals unity. Equation (2) reports the dimensionless form of the CR3BP equations in the MRF, where μ is the dimensionless ratio between the gravitational parameters, and $[\boldsymbol{r}_{em}]_m = [-1, 0, 0]^T$; in addition, Eq. (3) reports the relationship between dimensionless and dimensional quantities:

$$[\ddot{\boldsymbol{r}}]_m = -2[\Omega_{mi}]^m[\dot{\boldsymbol{r}}]_m - [\Omega_{mi}^2]^m[\boldsymbol{r}]_m - \mu\frac{[\boldsymbol{r}]_m}{r^3} - (1-\mu)\frac{[\boldsymbol{r}+\boldsymbol{r}_{em}]_m}{\|\boldsymbol{r}+\boldsymbol{r}_{em}\|^3} \tag{2}$$

$$\mu = \frac{\overline{\mu}_m/\overline{\mu}_e}{1+\overline{\mu}_m/\overline{\mu}_e}, \quad \overline{t} = \frac{t}{\overline{\omega}_{mi}}, \quad \overline{\boldsymbol{r}} = \overline{r}_{em}\boldsymbol{r},$$
$$\dot{\overline{\boldsymbol{r}}} = \overline{\omega}_{mi}\overline{r}_{em}\dot{\boldsymbol{r}}, \quad \ddot{\overline{\boldsymbol{r}}} = \overline{\omega}_{mi}^2\overline{r}_{em}\ddot{\boldsymbol{r}}, \quad \overline{\omega}_{mi} = \sqrt{\frac{\overline{\mu}_e+\overline{\mu}_m}{\overline{r}_{em}^3}} \tag{3}$$

The derivation of the relative motion equations in the VRF starts with the absolute motion representation reported in Eq. (3) and follows a similar approach to [20]. First, the target–chaser relative position vector ρ is defined as in Eq. (4), where x, y, and z are its components in the VRF, and $\boldsymbol{r}_c$ and $\boldsymbol{r}$ are the position vectors of the chaser and the target spacecraft:

$$[\boldsymbol{\rho}]_i = [\boldsymbol{r}_c]_i - [\boldsymbol{r}]_i = x[\hat{\boldsymbol{\imath}}]_i + y[\hat{\boldsymbol{\jmath}}]_i + z[\hat{\boldsymbol{k}}]_i \tag{4}$$

By differentiating Eq. (4) two times, the relative acceleration between the target and the chaser can be related to its expression in the VRF frame through the transport theorem as follows:

$$[\dot{\boldsymbol{\rho}}]_i = [\dot{\boldsymbol{r}}_c]_i - [\dot{\boldsymbol{r}}]_i = [\dot{\boldsymbol{\rho}}]_v^i + [\Omega_{vi}]^i[\boldsymbol{\rho}]_i \tag{5}$$

$$[\ddot{\boldsymbol{\rho}}]_i = [\ddot{\boldsymbol{r}}_c]_i - [\ddot{\boldsymbol{r}}]_i = [\ddot{\boldsymbol{\rho}}]_v^i + 2[\Omega_{vi}]^i[\dot{\boldsymbol{\rho}}]_v^i + [\dot{\Omega}_{vi}]_v^i[\boldsymbol{\rho}]_i + [\Omega_{vi}^2]^i[\boldsymbol{\rho}]_i \tag{6}$$

Substituting terms $[\ddot{\boldsymbol{r}}]_i$ and $[\ddot{\boldsymbol{r}}_c]_i$ in Eq. (6) as per Eq. (1), the nonlinear equations of relative motion as observed in the VRF are obtained. These are reported in Eq. (7) by considering that the angular velocity of the VRF with respect to the IRF and its derivative in time can be computed as per Eqs. (8) and (9):

$$[\ddot{\boldsymbol{\rho}}]_v^i + 2[\Omega_{vi}]^i[\dot{\boldsymbol{\rho}}]_v^i + [\dot{\Omega}_{vi}]_v^i[\boldsymbol{\rho}]_i + [\Omega_{vi}^2]^i[\boldsymbol{\rho}]_i$$
$$= \mu\left(\frac{[\boldsymbol{r}]_i}{r^3} - \frac{[\boldsymbol{r}+\boldsymbol{\rho}]_i}{\|\boldsymbol{r}+\boldsymbol{\rho}\|^3}\right) + (1-\mu)\left(\frac{[\boldsymbol{r}+\boldsymbol{r}_{em}]_i}{\|\boldsymbol{r}+\boldsymbol{r}_{em}\|^3} - \frac{[\boldsymbol{r}+\boldsymbol{r}_{em}+\boldsymbol{\rho}]_i}{\|\boldsymbol{r}+\boldsymbol{r}_{em}+\boldsymbol{\rho}\|^3}\right) \tag{7}$$

$$\boldsymbol{\omega}_{vi} = \boldsymbol{\omega}_{vm} + \boldsymbol{\omega}_{mi} \tag{8}$$

$$[\dot{\boldsymbol{\omega}}_{vi}]_v^i = [\dot{\boldsymbol{\omega}}_{vm}]_v^i + [\dot{\boldsymbol{\omega}}_{mi}]_v^i = [\dot{\boldsymbol{\omega}}_{vm}]_v^i + [\dot{\boldsymbol{\omega}}_{mi}]_m^i - [\Omega_{vm}]^i[\boldsymbol{\omega}_{mi}]^i \tag{9}$$

When the chaser and target spacecraft are sufficiently close (i.e., for $\rho/r \ll 1$), the linearization about the target orbit $\boldsymbol{r}(t)$ of Eq. (7) yields

$$[\ddot{\boldsymbol{\rho}}]_v + 2[\Omega_{vi}]^v[\dot{\boldsymbol{\rho}}]_v + [\dot{\Omega}_{vi}]_v[\boldsymbol{\rho}]_v + [\Omega_{vi}^2]^v[\boldsymbol{\rho}]_v$$
$$= -\frac{\mu}{r^3}\left(I_3 - 3\frac{[\boldsymbol{r}]_v[\boldsymbol{r}]_v^T}{r^2}\right)[\boldsymbol{\rho}]_v$$
$$-\frac{(1-\mu)}{\|\boldsymbol{r}+\boldsymbol{r}_{em}\|^3}\left(I_3 - 3\frac{[\boldsymbol{r}+\boldsymbol{r}_{em}]_v[\boldsymbol{r}+\boldsymbol{r}_{em}]_v^T}{\|\boldsymbol{r}+\boldsymbol{r}_{em}\|^2}\right)[\boldsymbol{\rho}]_v \tag{10}$$

As explained in [20], the quantities considered in Eqs. (8) and (9) can be expressed in analytical form. In fact, although $\boldsymbol{\omega}_{mi}$ and $\dot{\boldsymbol{\omega}}_{mi}$ are constant within the CR3BP formulation and equal to $\boldsymbol{\omega}_{mi} = [0, 0, 1]^T$ and $\dot{\boldsymbol{\omega}}_{mi} = [0, 0, 0]^T$, respectively, $\boldsymbol{\omega}_{vm}$ and $\dot{\boldsymbol{\omega}}_{vm}$ can be computed based on the knowledge of the state of the target spacecraft in the MRF. From the definition of the unit vectors of the VRF axes provided in Eq. (11), where v and h are the norms of vectors $[\dot{\boldsymbol{r}}]_m^i$ and $[\boldsymbol{r}]_i \times [\dot{\boldsymbol{r}}]_m^i$, respectively, the transport theorem can be applied to obtain Eq. (12) (see details in [20]):

$$[\hat{\boldsymbol{\imath}}]_i = [\hat{\boldsymbol{\jmath}}]_i \times [\hat{\boldsymbol{k}}]_i, \quad [\hat{\boldsymbol{\jmath}}]_i = \frac{[\dot{\boldsymbol{r}}]_m^i}{\|[\dot{\boldsymbol{r}}]_m^i\|} = \frac{[\dot{\boldsymbol{r}}]_m^i}{v}, \quad [\hat{\boldsymbol{k}}]_i = \frac{[\boldsymbol{h}]_m^i}{h} = \frac{[\boldsymbol{r}]_i \times [\dot{\boldsymbol{r}}]_m^i}{\|[\boldsymbol{r}]_i \times [\dot{\boldsymbol{r}}]_m^i\|} \tag{11}$$

$$[\hat{\boldsymbol{\imath}}]_i \times [\hat{\boldsymbol{\imath}}]_m^i + [\hat{\boldsymbol{\jmath}}]_i \times [\hat{\boldsymbol{\jmath}}]_m^i + [\hat{\boldsymbol{k}}]_i \times [\hat{\boldsymbol{k}}]_m^i = 2[\boldsymbol{\omega}_{vm}]^i \tag{12}$$

Therefore, explicitly evaluating vectors $[\dot{\hat{\boldsymbol{\imath}}}]_m^i$, $[\dot{\hat{\boldsymbol{\jmath}}}]_m^i$, and $[\dot{\hat{\boldsymbol{k}}}]_m^i$ allows one to find analytical expressions for the components of $\boldsymbol{\omega}_{vm}$ directly in the VRF [20]. Once vector $\boldsymbol{\omega}_{vm}$ is found, its components can be derived to find the corresponding angular acceleration as expressed in the VRF. Based on Eq. (11), unit vector $[\dot{\hat{\boldsymbol{\jmath}}}]_m^i$ can be computed as follows:

$$\left[\dot{\hat{\boldsymbol{\jmath}}}\right]_m^i = \frac{[\ddot{\boldsymbol{r}}]_m^i v - [\dot{\boldsymbol{r}}]_m^i \dot{v}}{v^2} = \frac{1}{v}\left([\ddot{\boldsymbol{r}}]_m^i - \dot{v}[\hat{\boldsymbol{\jmath}}]_i\right)$$
$$= \frac{1}{v}\left\{([\ddot{\boldsymbol{r}}]_m^i \cdot [\hat{\boldsymbol{\imath}}]_i)[\hat{\boldsymbol{\imath}}]_i + ([\ddot{\boldsymbol{r}}]_m^i \cdot [\hat{\boldsymbol{k}}]_i)[\hat{\boldsymbol{k}}]_i\right\} \tag{13}$$

where $\dot{v}$ is the projection of the acceleration vector along the y axis of the VRF:

$$\dot{v} = [\ddot{\boldsymbol{r}}]_v^i \cdot [\hat{\boldsymbol{\jmath}}]_i = ([\ddot{\boldsymbol{r}}]_m^i - [\Omega_{vm}]^i[\dot{\boldsymbol{r}}]_m^i) \cdot [\hat{\boldsymbol{\jmath}}]_i = [\ddot{\boldsymbol{r}}]_m^i \cdot [\hat{\boldsymbol{\jmath}}]_i \tag{14}$$

Similarly, vector $[\dot{\hat{\boldsymbol{k}}}]_m^i$ can be expressed as

$$\left[\dot{\hat{\boldsymbol{k}}}\right]_m^i = \frac{[\dot{\boldsymbol{h}}]_m^i - \dot{h}[\hat{\boldsymbol{k}}]_i}{h} = \frac{1}{h}\left\{[\dot{\boldsymbol{h}}]_m^i - ([\dot{\boldsymbol{h}}]_m^i \cdot [\hat{\boldsymbol{k}}]_i)[\hat{\boldsymbol{k}}]_i\right\}$$
$$= \frac{1}{h}\left\{([\dot{\boldsymbol{h}}]_m^i \cdot [\hat{\boldsymbol{\imath}}]_i)[\hat{\boldsymbol{\imath}}]_i + ([\dot{\boldsymbol{h}}]_m^i \cdot [\hat{\boldsymbol{\jmath}}]_i)[\hat{\boldsymbol{\jmath}}]_i\right\} \tag{15}$$

where $\dot{h}$ is the projection of the time derivative of the orbit angular momentum vector along the z axis of the VRF:

$$\dot{h} = [\dot{\boldsymbol{h}}]_v^i \cdot [\hat{\boldsymbol{k}}]_i = \left([\dot{\boldsymbol{h}}]_m^i - [\Omega_{vm}]^i[\boldsymbol{h}]_v^i\right) \cdot [\hat{\boldsymbol{k}}]_i = [\dot{\boldsymbol{h}}]_m^i \cdot [\hat{\boldsymbol{k}}]_i \tag{16}$$

As a result, applying the rule of the derivative of a product to the expression of $[\hat{\boldsymbol{\imath}}]_i$ in Eq. (11) and substituting Eqs. (13) and (15), the following result is obtained:

$$[\dot{\hat{\boldsymbol{\imath}}}]_m^i = [\dot{\hat{\boldsymbol{\jmath}}}]_m^i \times [\hat{\boldsymbol{k}}]_i - [\dot{\hat{\boldsymbol{k}}}]_m^i \times [\hat{\boldsymbol{\jmath}}]_i$$
$$= -\frac{1}{v}([\ddot{\boldsymbol{r}}]_m^i \cdot [\hat{\boldsymbol{\imath}}]_i)[\hat{\boldsymbol{\jmath}}]_i - \frac{1}{h}\left([\dot{\boldsymbol{h}}]_m^i \cdot [\hat{\boldsymbol{\imath}}]_i\right)[\hat{\boldsymbol{k}}]_i \tag{17}$$

Equations (13–17) represent the derivatives of the directions of the VRF axes expressed in the VRF. Combining these results in Eq. (12), then $\boldsymbol{\omega}_{vm}$ can be expressed in terms of its components along the VRF axes as per Eq. (18):

$$[\boldsymbol{\omega}_{vm}]^i = \left(\frac{1}{2v}[\ddot{\boldsymbol{r}}]^i_m \cdot [\widehat{\boldsymbol{k}}]_i - \frac{1}{2h}[\dot{\boldsymbol{h}}]^i_m \cdot [\hat{\boldsymbol{j}}]_i\right)[\hat{\boldsymbol{i}}]_i + \left(\frac{1}{h}[\dot{\boldsymbol{h}}]^i_m \cdot [\hat{\boldsymbol{i}}]_i\right)[\hat{\boldsymbol{j}}]_i + \left(-\frac{1}{v}[\ddot{\boldsymbol{r}}]^i_m \cdot [\hat{\boldsymbol{i}}]_i\right)[\widehat{\boldsymbol{k}}]_i \tag{18}$$

The components of $\boldsymbol{\omega}_{vm}$ along the VRF axes can be developed further from Eq. (18) by explicating the dot products. Borrowing the following definition of $\dot{r}$ from [20],

$$\dot{r} = \frac{1}{r}[\boldsymbol{r}]_i \cdot [\dot{\boldsymbol{r}}]^i_m \tag{19}$$

the dot products in Eq. (18) can be explicated as follows:

$$\begin{aligned}[\ddot{\boldsymbol{r}}]^i_m \cdot [\hat{\boldsymbol{i}}]_i &= [\ddot{\boldsymbol{r}}]^i_m \cdot ([\hat{\boldsymbol{j}}]_i \times [\widehat{\boldsymbol{k}}]_i)\\ &= \frac{1}{hv}[\ddot{\boldsymbol{r}}]^i_m \cdot \{([\dot{\boldsymbol{r}}]^i_m \cdot [\dot{\boldsymbol{r}}]^i_m)[\boldsymbol{r}]_i - ([\dot{\boldsymbol{r}}]^i_m \cdot [\boldsymbol{r}]_i)[\dot{\boldsymbol{r}}]^i_m\}\\ &= \frac{v}{h}([\ddot{\boldsymbol{r}}]^i_m \cdot [\boldsymbol{r}]_i) - \frac{r\dot{r}}{hv}([\ddot{\boldsymbol{r}}]^i_m \cdot [\dot{\boldsymbol{r}}]^i_m)\end{aligned} \tag{20}$$

$$[\ddot{\boldsymbol{r}}]^i_m \cdot [\widehat{\boldsymbol{k}}]_i = [\ddot{\boldsymbol{r}}]^i_m \cdot ([\boldsymbol{r}]_i \times [\dot{\boldsymbol{r}}]^i_m) \tag{21}$$

$$\begin{aligned}[\dot{\boldsymbol{h}}]^i_m \cdot [\hat{\boldsymbol{i}}]_i &= ([\boldsymbol{r}]_i \times [\ddot{\boldsymbol{r}}]^i_m) \cdot ([\hat{\boldsymbol{j}}]_i \times [\widehat{\boldsymbol{k}}]_i)\\ &= ([\boldsymbol{r}]_i \cdot [\hat{\boldsymbol{j}}]_i)([\ddot{\boldsymbol{r}}]^i_m \cdot [\widehat{\boldsymbol{k}}]_i) - ([\boldsymbol{r}]_i \cdot [\widehat{\boldsymbol{k}}]_i)([\ddot{\boldsymbol{r}}]^i_m \cdot [\hat{\boldsymbol{j}}]_i)\\ &= \frac{r\dot{r}}{hv}[\ddot{\boldsymbol{r}}]^i_m \cdot [\boldsymbol{h}]^i_m\end{aligned} \tag{22}$$

$$[\dot{\boldsymbol{h}}]^i_m \cdot [\hat{\boldsymbol{j}}]_i = ([\boldsymbol{r}]_i \times [\ddot{\boldsymbol{r}}]^i_m) \cdot \frac{[\dot{\boldsymbol{r}}]^i_m}{v} = -\frac{1}{v}[\ddot{\boldsymbol{r}}]^i_m \cdot [\boldsymbol{h}]^i_m \tag{23}$$

As a result, by substituting Eqs. (20–23) into Eq. (18), vector $\boldsymbol{\omega}_{vm}$ can be expressed in the VRF as shown in Eq. (24) as a function of quantities related to the absolute motion of the target object:

$$\begin{aligned}[\boldsymbol{\omega}_{vm}]^v &= \omega^v_{vm,x}\hat{\boldsymbol{i}} + \omega^v_{vm,y}\hat{\boldsymbol{j}} + \omega^v_{vm,z}\widehat{\boldsymbol{k}}\\ &= \left(\frac{1}{hv}[\ddot{\boldsymbol{r}}]^i_m \cdot [\boldsymbol{h}]^i_m\right)\hat{\boldsymbol{i}} + \left(\frac{r\dot{r}}{h^2v}[\ddot{\boldsymbol{r}}]^i_m \cdot [\boldsymbol{h}]^i_m\right)\hat{\boldsymbol{j}}\\ &\quad + \left(-\frac{1}{h}[\ddot{\boldsymbol{r}}]^i_m \cdot [\boldsymbol{r}]_i + \frac{r\dot{r}}{hv^2}[\ddot{\boldsymbol{r}}]^i_m \cdot [\dot{\boldsymbol{r}}]^i_m\right)\widehat{\boldsymbol{k}}\end{aligned} \tag{24}$$

By directly differentiating the VRF components of vector $\boldsymbol{\omega}_{vm}$, the components $\dot{\omega}^v_{vm,x}$, $\dot{\omega}^v_{vm,y}$, and $\dot{\omega}^v_{vm,z}$ of vector $\dot{\boldsymbol{\omega}}_{vm}$ expressed in the same frame can be obtained:

$$\begin{aligned}\dot{\omega}^v_{vm,x} &= -\left(\frac{\dot{h}}{h} + \frac{\dot{v}}{v}\right)\omega^v_{vm,x} + \frac{1}{hv}[\dddot{\boldsymbol{r}}]^i_m \cdot [\boldsymbol{h}]^i_m\\ \dot{\omega}^v_{vm,y} &= \left(\frac{\dot{r}}{r} - \frac{\dot{v}}{v} - \frac{2\dot{h}}{h}\right)\omega^v_{vm,y} + \frac{r\ddot{r}}{h}\omega^v_{vm,x} + \frac{r\dot{r}}{h^2v}[\ddot{\boldsymbol{r}}]^i_m \cdot [\boldsymbol{h}]^i_m\\ \dot{\omega}^v_{vm,z} &= -\frac{\dot{h}}{h}\omega^v_{vm,z} - \frac{1}{h}[\dddot{\boldsymbol{r}}]^i_m \cdot [\boldsymbol{r}]_i\\ &\quad + \left(\left(\frac{\dot{r}}{r} - \frac{2\dot{v}}{v}\right)\frac{r\dot{r}}{hv^2} + \frac{r\ddot{r}}{hv^2} - \frac{1}{h}\right)[\ddot{\boldsymbol{r}}]^i_m \cdot [\dot{\boldsymbol{r}}]^i_m\\ &\quad + \frac{r\dot{r}}{hv^2}\left([\ddot{\boldsymbol{r}}]^i_m \cdot [\dot{\boldsymbol{r}}]^i_m + \|[\ddot{\boldsymbol{r}}]^i_m\|^2\right)\end{aligned} \tag{25}$$

in which $\ddot{r}$ can be obtained by directly differentiating $\dot{r}$, and the jerk term $[\dddot{\boldsymbol{r}}]^i_m$ can be obtained as per Eq. (26) by direct derivation of the target acceleration expressed as in Eq. (2), with the useful notation for the derivative of the terms $\boldsymbol{p}/p^3$ borrowed from [20]:

$$\begin{aligned}[\dddot{\boldsymbol{r}}]^i_m &= -2[\Omega_{mi}]^i[\ddot{\boldsymbol{r}}]^i_m - [\Omega^2_{mi}]^i[\dot{\boldsymbol{r}}]^i_m - \mu\frac{\partial}{\partial \boldsymbol{r}}\left[\frac{[\boldsymbol{r}]_i}{r^3}\right][\dot{\boldsymbol{r}}]^i_m\\ &\quad - (1-\mu)\frac{\partial}{\partial \boldsymbol{r}}\left[\frac{[\boldsymbol{r}+\boldsymbol{r}_{em}]_i}{\|\boldsymbol{r}+\boldsymbol{r}_{em}\|^3}\right][\dot{\boldsymbol{r}}]^i_m,\\ \frac{\partial}{\partial \boldsymbol{p}}\left[\frac{\boldsymbol{p}}{p^3}\right] &= \frac{1}{p^3}\left(I_3 - 3\frac{\boldsymbol{p}\boldsymbol{p}^T}{p^2}\right)\end{aligned} \tag{26}$$

The proposed model can be used to propagate relative dynamics by direct integration of either the nonlinear [Eq. (7)] and linearized [Eq. (10)] equations in conjunction with the absolute dynamics equations [Eq. (2)] of the target object. However, it is useful to rewrite Eq. (10) in the form of a linear time-varying system as shown in Eq. (27), in which the state vector is $\boldsymbol{x} = [[\boldsymbol{\rho}]^T_v, [\dot{\boldsymbol{\rho}}]^T_v]^T$, and the control actions vector $\boldsymbol{u}$ has its components expressed along the VRF axes:

$$\dot{\boldsymbol{x}} = A(t)\boldsymbol{x} + B\boldsymbol{u}, \quad A(t) = \begin{bmatrix} 0_3 & I_3 \\ A_v(t) & -2[\Omega_{vi}(t)]^v \end{bmatrix}, \quad B = \begin{bmatrix} 0_3 \\ I_3 \end{bmatrix} \tag{27}$$

$$\begin{aligned}A_v(t) &= -[\dot{\Omega}_{vi}]_v - [\Omega^2_{vi}]^v - \frac{\mu}{r^3}\left(I_3 - 3\frac{[\boldsymbol{r}]_v[\boldsymbol{r}]^T_v}{r^2}\right)\\ &\quad - \frac{(1-\mu)}{\|\boldsymbol{r}+\boldsymbol{r}_{em}\|^3}\left(I_3 - 3\frac{[\boldsymbol{r}+\boldsymbol{r}_{em}]_v[\boldsymbol{r}+\boldsymbol{r}_{em}]^T_v}{\|\boldsymbol{r}+\boldsymbol{r}_{em}\|^2}\right)\end{aligned} \tag{28}$$

Matrix $A(t)$ is the Jacobian of Eq. (10) and is periodic with the same period τ of the target orbit: therefore, Eqs. (27) and (28) represent a periodic LTV system if the orbit of the target spacecraft is periodic. This formulation also allows introducing additional terms, like the gravitational acceleration of a fourth body or the solar radiation pressure acceleration in A_v, or as part of the input $\boldsymbol{u}$ [18], as long as the linearization remains valid.

III. Modal Decomposition of the Relative Motion in the CR3BP

The method of fundamental modal solutions presented in [33,34] is applied to the periodic LTV system shown in Eqs. (27) and (28) to gain further insight into the geometry of the motion. The application of the method requires that the LF transformation matrix $P(t)$ is identified, defining the instantaneous change of coordinates $\boldsymbol{x}(t) = P(t)\boldsymbol{z}(t)$ between the original LTV system state $\boldsymbol{x}$ and the equivalent LTI system state $\boldsymbol{z}$. In the following, a summary of the relevant mathematical definitions exploited in this work is provided; additional details and mathematical derivations are available in [32–35].

A. Mathematical Background

Given a periodic LTV system with period τ, fundamental matrix equation (29) describes the evolution of its state transition matrix $\Phi(t, t_0)$ from the initial time t_0 to time t, and it is such that $\Phi(t_0, t_0) = I_6$. A solution to this equation can be written using matrix $P(t)$ as in Eq. (30), where matrix Λ has constant complex entries and must satisfy the condition shown in Eq. (31) [33,34]:

$$\dot{\Phi}(t, t_0) = A(t)\Phi(t, t_0) \tag{29}$$

$$\Phi(t, t_0) = P(t)e^{\Lambda(t-t_0)} \tag{30}$$

$$P^{-1}(t)(A(t)P(t) - \dot{P}(t)) = \Lambda(t) \tag{31}$$

In accordance with previous works [32–35], the transformation $P(t)$ is obtained as in Eq. (32) by inverting Eq. (30), yielding a periodic matrix with period τ and equal to the identity matrix after positive integer multiples of τ. However, Eq. (32) shows that knowledge of matrix Λ is required to evaluate matrix $P(t)$. Therefore, evaluating Eq. (30) at time $t_0 + \tau$ allows computing the monodromy

matrix $\Phi(t_0+\tau,t_0)=M$, from which matrix Λ can be obtained as per Eq. (33). In this equation, the natural logarithm of a matrix is defined as the principal matrix logarithm (i.e., the inverse transformation of the matrix exponential):

$$P(t)=\Phi(t,t_0)e^{-\Lambda(t-t_0)},\quad P(t_0)=P(t_0+k\tau)=I_6,\quad k\in\mathbb{Z}^+ \tag{32}$$

$$M=P(t_0+\tau)e^{\Lambda\tau}=I_6e^{\Lambda\tau}\Rightarrow\Lambda=\frac{1}{\tau}\log M \tag{33}$$

The equivalent LTI system obtained by transforming the original LTV system of Eq. (27) is shown in Eq. (34), and it is obtained by considering that Eq. (31) defines matrix Λ. The first term in the right-hand side of the equation is the direct transformation of the homogeneous equation of the LTV system, and the second term directly results from Eq. (27) when the coordinate transformation between $\boldsymbol{x}$ and $\boldsymbol{z}$ is applied [35]. Notably, Eq. (34) has also been observed by Cuevas del Valle et al. [36] in their work:

$$\dot{\boldsymbol{z}}=\Lambda\boldsymbol{z}+P^{-1}(t)B\boldsymbol{u} \tag{34}$$

The modal decomposition is finally applied to the equivalent LTI system in which $\boldsymbol{u}=\boldsymbol{0}$, and the first step is decomposing matrix Λ in its Jordan normal form and evaluating its normalized eigenvalues and eigenvectors. In this respect, Eq. (35) holds true and is derived by Eq. (33). In the equation, the columns of matrices V_λ and V_m are the eigenvectors of matrices Λ and M, respectively, and diagonal matrices J_λ and J_m contain the eigenvalues of Λ and M:

$$M=V_mJ_mV_m^{-1}\Leftrightarrow\Lambda=V_m\left(\frac{1}{T}\log(J_m)\right)V_m^{-1}=V_\lambda J_\lambda V_\lambda^{-1} \tag{35}$$

Each eigenvalue λ_i and associated eigenvector $\boldsymbol{v}_i$ of Λ allow definition of a fundamental solution to Eq. (34) with null $\boldsymbol{u}$ in the form $\boldsymbol{\zeta}_i(t)=\boldsymbol{v}_ie^{\lambda_i(t-t_0)}$, representing a portion of the motion (i.e., a mode), which can be converted to a fundamental solution of the LTV system of Eq. (27). By linearly combining the fundamental solutions through the set of coefficients $\boldsymbol{c}=[c_1,c_2,\ldots,c_6]^T$, any solution can be described. If the fundamental solutions are grouped as the columns of a matrix $Z(t)$, then the general solution $\boldsymbol{x}(t)$ of Eq. (27) can be represented as in Eq. (36), and the initial conditions $\boldsymbol{x}(t_0)=\boldsymbol{x}_0$ can be related to the corresponding set of coefficients $\boldsymbol{c}$ through the relation $\boldsymbol{x}_0=V_\lambda\boldsymbol{c}$. Notably, Eq. (36) highlights that any LTV solution is a combination of the LTI ones $\boldsymbol{z}_i=c_i\boldsymbol{\zeta}_i(t)$ weighted by the rows of $P(t)$, which change over time as described in Eq. (32):

$$\boldsymbol{x}(t)=\Psi(t)\boldsymbol{c}=P(t)Z(t)\boldsymbol{c}=\sum_{i=1}^{6}c_iP(t)\boldsymbol{v}_ie^{\lambda_i(t-t_0)} \tag{36}$$

B. Common Fundamental Modal Solutions and Their Refactorization

The terms in Eq. (36) can assume complex values; however, it is possible to retain an equivalent, fully real formulation of this equation if the fundamental solutions related to complex conjugate eigenvalues are refactored. In the following, common results are recollected that occur when analyzing LTV systems and, specifically, the relative dynamics in the CR3BP problem.

As Burnett and Schaub highlighted in [34], if the orbit of the target in the CR3BP problem is perfectly periodic, then Λ has a null defective eigenvalue, having algebraic multiplicity of two (i.e., two eigenvalues λ_i and λ_j are identical and equal to zero) and geometric multiplicity of one (i.e., one linearly independent eigenvector is associated to it). Therefore, a generalized eigenvector $\boldsymbol{v}_j$ can be computed from $\boldsymbol{v}_i$, and the solution of Eq. (27) associated with the null defective eigenvalues can be expressed as in Eq. (37). This solution represents a trivial mode in which the motion is described by an offset term and a component drifting linearly with time. Notably, both eigenvectors are necessarily real because matrix M and the two corresponding eigenvalues are real as well:

$$\boldsymbol{z}_{ij}(t)=c_i\boldsymbol{v}_i+c_j(\boldsymbol{v}_i(t-t_0)+\boldsymbol{v}_j) \tag{37}$$

The modes associated with purely real eigenvalues of Λ (i.e., stable and unstable modes) are fully real in their description too because the corresponding eigenvectors must be real themselves. Therefore, given a real eigenvalue λ_i and the corresponding eigenvector $\boldsymbol{v}_i$, a stable or unstable mode is straightforwardly described by Eq. (38):

$$\boldsymbol{z}_i(t)=c_i\boldsymbol{v}_ie^{\lambda_i(t-t_0)} \tag{38}$$

Center modes are associated to couples of conjugate imaginary eigenvalues $\lambda_i=-i\omega_i$ and $\lambda_j=+i\omega_i$, and the corresponding eigenvectors retain imaginary parts. Following the prescriptions given in [33,34], the fundamental solutions associated with each conjugate eigenvalue can be refactored together to remove the imaginary part. To this purpose, the two coefficients and eigenvectors are rewritten as a combination of their real and imaginary parts as $c_{i,j}=c_R\pm ic_I$ and $\boldsymbol{v}_{i,j}=\boldsymbol{v}_R\pm i\boldsymbol{v}_I$, and the solutions are summed together to find the purely real form expressed in Eq. (39). When this refactorization is considered, the set of coefficients $\boldsymbol{c}$ and the matrix of eigenvectors V_λ must be modified to include coefficients c_R and c_I instead of c_i and c_j, and column vectors $2\boldsymbol{v}_R$ and $-2\boldsymbol{v}_I$ instead of $\boldsymbol{v}_i$ and $\boldsymbol{v}_j$. Notably, the motion represented in Eq. (39) is periodic with period $2\pi/\omega_k$, which is not necessarily commensurate with the period of the orbit of the target object. Therefore, when Eq. (39) is multiplied by matrix $P(t)$ to obtain the Cartesian representation of the motion in the LTV state space, the resulting motion is typically a quasi-periodic one:

$$\begin{aligned}\boldsymbol{z}_{ij}(t)&=c_R[2\boldsymbol{v}_R\cos(\omega_k(t-t_0))-2\boldsymbol{v}_I\sin(\omega_k(t-t_0))]\\&\quad-c_I[2\boldsymbol{v}_R\sin(\omega_k(t-t_0))+2\boldsymbol{v}_I\cos(\omega_k(t-t_0))]\\&=c_R\boldsymbol{\zeta}_i(t)+c_I\boldsymbol{\zeta}_j(t)\end{aligned} \tag{39}$$

Finally, it is possible that the eigenvalues of center modes exist that are characterized by real and complex parts approaching zero. In these cases, given the general result $\boldsymbol{z}_i(t)=c_i\boldsymbol{v}_ie^{(\lambda_R+i\lambda_I)(t-t_0)}$, the LTI function can be approximated as $\boldsymbol{z}_i(t)\approx c_i\boldsymbol{v}_i$ for small values of the exponent, which occurs over a time interval $t-t_0$ that becomes larger as the magnitudes of λ_R and λ_I become smaller. Considering the two center modes simultaneously, a refactorization can be performed as in the case of any other center mode; as opposed to the general expression of the solution, the refactorization allows one to retain the real part only and results in a time-invariant function $\boldsymbol{z}_{ij}$.

C. Geometrical Analysis of the Modes of Motion

The refactored solutions in Eqs. (37–39) show that the LTI equivalent of the LTV system solution obtained through modal decomposition can be given a geometrical interpretation if the equations are further manipulated. This interpretation can be extended to the original LTV system as well if the periodicity of the LF transformation matrix $P(t)$ is considered. In the following, the common types of modes discussed in Sec. III.B are considered separately, focusing on the stable, unstable, and center ones. The trivial mode shave a directly interpretable geometrical meaning, as they represent an offset term with a linear drift in time, to which an oscillatory behavior is superimposed due to the periodicity of $P(t)$. Moreover, given that $P(t_0)=I_6$, for any mode the last three entries of vector $\boldsymbol{z}_i(t_0)$ represent the initial velocity of the motion and thus indicate the initial direction of evolution of the ith mode.

1. Analysis in the LTI State Space

In the case of stable and unstable modes, Eq. (38) can be rewritten as in Eq. (40) by considering that the initial condition of the motion (i.e., $\boldsymbol{z}_i(t_0) = c_i \boldsymbol{v}_i e^{-\lambda_i t_0}$) is the scaling factor of the exponential term. Moreover, in stable and unstable modes, the direction of motion can also be obtained as the unit vector computed using the last three entries of eigenvector $\boldsymbol{v}_i$:

$$\boldsymbol{z}_i(t) = c_i \boldsymbol{\alpha}_i e^{\lambda_i t}, \quad \boldsymbol{\alpha}_i = \boldsymbol{v}_i / e^{\lambda_i t_0} \tag{40}$$

If a couple of center modes with eigenvalues $\lambda_{i,j} = \mp i\omega_i$ are considered, Eq. (39) shows that each refactored mode can be seen as a vector of harmonic oscillators as per Eq. (41), in which $z_{p,m}(t)$ is the mth component of the pth fundamental solution $\boldsymbol{z}_p(t)$, with $p = i, j$. The amplitude $\overline{a}_{p,m}$ of each oscillator is thus a function of the modal coefficients and the elements of the corresponding eigenvectors, whereas the phase ϕ_{vijm} is a function of the elements of the eigenvectors only:

$$\begin{aligned}
&z_{i,m}(t) = \overline{a}_{i,m} \cos(\omega_i t - \phi_{0i} + \phi_{v_{ij}m}),\\
&z_{j,m}(t) = \overline{a}_{j,m} \sin(\omega_i t - \phi_{0i} + \phi_{v_{ij}m})\\
&\overline{a}_{p,m} = c_p \sqrt{v_{i,m}^2 + v_{j,m}^2} = c_p v_{ij,m}, \quad p = i, j,\\
&\phi_{0i} = \omega_i t_0, \quad \phi_{v_{ij}m} = \tan^{-1}\left(\frac{v_{j,m}}{v_{i,m}}\right)
\end{aligned} \tag{41}$$

Equation (41) highlights that the sine and cosine functions of the two modes share the same argument; therefore, the motion $\boldsymbol{z}_{ij}(t)$ associated with the combination of the two harmonic oscillators can also be expressed as a harmonic oscillator as per Eq. (42). From a geometrical perspective, Eq. (42) clarifies that any oscillatory motion in the LTI state space is bounded and represented by a three-dimensional ellipse described by the corresponding modal coefficients, which can thus be interpreted as design variables:

$$\begin{aligned}
&z_{ij,m}(t) = \overline{a}_{ij,m} \sin(\omega_i t - \phi_{0i} + \phi_{v_{ij}m} + \phi_{c_{ij}})\\
&\overline{a}_{ij,m} = v_{ij,m} \sqrt{c_i^2 + c_j^2}, \phi_{c_{ij}} = \tan^{-1}(\overline{a}_{i,m}/\overline{a}_{j,m}) = \tan^{-1}(c_i/c_j)
\end{aligned} \tag{42}$$

2. Extension to the LTV State Space

The extension of these concepts to the Cartesian state representation of the LTV formulation is complicated by the presence of the periodicity of the $P(t)$ matrix, periodic with the same period τ of the target spacecraft trajectory. In fact, the jth component of the Cartesian state $\boldsymbol{x}$ results from a combination of all components of vector $\boldsymbol{z}$ according to the elements of the jth row $\boldsymbol{p}_{r,j}(t)$ of matrix $P(t)$. This time-varying combination cannot be modeled analytically in the context of the CR3BP; nevertheless, useful relations can still be derived between the coefficients $\boldsymbol{c}$ and the geometrical properties of the motion by analyzing each mode numerically. Notably, numerical analyses can be performed once and over a time span limited to a few orbital periods of the target thanks to the periodicity of $P(t)$.

In the case of the stable and unstable modes, the Cartesian relative state for the generic ith mode can be represented as follows:

$$\boldsymbol{x}_i(t) = c_i \boldsymbol{p}_s(t) e^{\lambda_i t}, \quad \boldsymbol{p}_s(t) = [\boldsymbol{p}_{r,1}^T(t)\,\boldsymbol{\alpha}_i, \ldots, \boldsymbol{p}_{r,6}^T(t)\,\boldsymbol{\alpha}_i]^T \tag{43}$$

Equation (43) can be analyzed both componentwise and in terms of its norm. First, observing that each component of vector $\boldsymbol{z}_i$ in Eq. (40) is a monotone exponential function, the superior and inferior limits of the mth component of the motion as functions of time can be expressed as in Eqs. (44) and (45). Consequently, the norm of the relative position vector ρ_i associated with the ith mode follows the same exponential trend while oscillating with period τ. The superior and inferior limits as functions of time are evaluated as in Eqs. (46) and (47), and they describe the bounds of the motion of the stable or unstable mode. These expressions can thus be used to describe a control-free approaching or departing trajectory with respect to the target spacecraft, respectively. The design of such motion can be performed by selecting the value of the corresponding modal coefficient that allows achievement of a desired minimum target–chaser separation $\rho_{\text{inf},i}(t_f)$ at a given final time t_f. Notably, the sign of the coefficient does not affect the evolution of functions $\rho_{\text{inf},i}(t)$ and $\rho_{\text{sup},i}(t)$, and it must be chosen depending on the direction from which the chaser is approaching the target, based on the sign of the elements of the first three entries of the eigenvector $\boldsymbol{v}_i$:

$$\begin{aligned}
&x_{\text{inf},i,m}(t) = |c_i| b_{v_i,m} e^{\lambda_i t} \le c_i \left(\boldsymbol{p}_{r,m}^T(t)\boldsymbol{\alpha}_i\right) e^{\lambda_i t}\\
&b_{v_i,m} = \min_{t\in[t_0,t_0+T]} \left(\text{sign}(c_i)\boldsymbol{p}_{r,m}^T(t)\boldsymbol{\alpha}_i\right) \quad , \quad m = 1,\ldots,6
\end{aligned} \tag{44}$$

$$\begin{aligned}
&x_{\text{sup},i,m}(t) = |c_i| l_{v_i,m} e^{\lambda_i t} \ge c_i \left(\boldsymbol{p}_{r,m}^T(t)\boldsymbol{\alpha}_i\right) e^{\lambda_i t}\\
&l_{v_i,m} = \max_{t\in[t_0,t_0+T]} \left(\text{sign}(c_i)\boldsymbol{p}_{r,m}^T(t)\boldsymbol{\alpha}_i\right) \quad , \quad m = 1,\ldots,6
\end{aligned} \tag{45}$$

$$\begin{aligned}
&\rho_{\text{inf},i}(t) = |c_i| d_{\rho,m} e^{\lambda_i t},\\
&d_{\rho,m} = \min\left(\sqrt{b_{v_i,1}^2 + b_{v_i,2}^2 + b_{v_i,3}^2}, \sqrt{l_{v_i,1}^2 + l_{v_i,2}^2 + l_{v_i,3}^2}\right)
\end{aligned} \tag{46}$$

$$\begin{aligned}
&\rho_{\text{sup},i}(t) = |c_i| d_{\rho,M} e^{\lambda_i t},\\
&d_{\rho,M} = \max\left(\sqrt{b_{v_i,1}^2 + b_{v_i,2}^2 + b_{v_i,3}^2}, \sqrt{l_{v_i,1}^2 + l_{v_i,2}^2 + l_{v_i,3}^2}\right)
\end{aligned} \tag{47}$$

In case a couple of center modes are considered, the Cartesian relative state during the motion is bounded, and it is possible to relate the expected maximum and minimum target–chaser separations to the modal coefficients. To this purpose, each mth component of the motion can be expressed as the product of two vectors of periodic functions with different periods, as in Eq. (48): specifically, the components of vector $\boldsymbol{p}_{r,m}(t)$ have period τ, whereas the components of vector $\boldsymbol{s}_{ij}(t)$ have period equal to $\tau_i = 2\pi/\omega_i$. Because periods τ and τ_i are usually incommensurate, the norm $\rho_{ij}(t)$ of the relative position vector behaves like a quasi-periodic function. Therefore, searching for the superior and inferior limits of the motion requires numerically computing the maximum and minimum values of $\rho_{ij}(t)$ as per Eq. (49), where τ_f is the smallest temporal interval over which the maximum and minimum shall be computed. The latter is taken as the closest larger integer multiple of period τ that approximates τ_i; in this way, approximations of the superior and inferior limits can be computed easily while considering the quasi-periodicity of the motion:

$$\begin{aligned}
&x_{ij,m}(t) = \left(\sqrt{c_i^2 + c_j^2}\right) \boldsymbol{p}_{r,m}^T(t) \boldsymbol{s}_{ij}(t),\\
&\boldsymbol{s}_{ij}(t) = \begin{bmatrix} v_{ij,1} \sin(\omega_i t - \phi_{0i} + \phi_{v_{ij}1} + \phi_{c_{ij}}) \\ \vdots \\ v_{ij,6} \sin(\omega_i t - \phi_{0i} + \phi_{v_{ij}6} + \phi_{c_{ij}}) \end{bmatrix}
\end{aligned} \tag{48}$$

$$\begin{aligned}
&\rho_{\text{inf},ij} = \min_{t\in[t_0,t_0+\tau_f]} \rho_{ij}(t)\\
&\rho_{\text{sup},ij} = \max_{t\in[t_0,t_0+\tau_f]} \rho_{ij}(t)
\end{aligned} \quad , \quad \rho_{ij}(t) = \sqrt{x_{ij,1}^2(t) + x_{ij,2}^2(t) + x_{ij,3}^2(t)},$$

$$\tau_f = \text{ceil}\left(\frac{\tau_i}{\tau}\right)\tau_i \tag{49}$$

The minimum of function $\rho_{ij}(t)$ can be expressed as in Eq. (50), which is a relationship between the coefficients of the center modes

and the minimum admissible target–chaser separation. From a geometrical perspective, the latter represents a spherical keep-out zone of radius $\rho_{\text{inf},ij} = r_{\text{KOZ}}$, and Eq. (50) can thus be used to design a trajectory that meets this constraint. However, Eq. (50) requires an iterative resolution of the problem due to $m_{ij,\min}$ being dependent on coefficients c_i and c_j, and it can only provide one constraint, thus leaving space for a second constraint to be applied to fix the value of the other coefficient. In this respect, if c_i is constrained to be zero, then the term $\phi_{c_{ij}}$ in the elements of vector $\boldsymbol{s}_{ij}(t)$ of Eq. (48) can be nullified. In doing so, the coefficient $m_{ij,\min}$ of Eq. (50) becomes constant for different values of c_j, and Eq. (50) can be inverted to find the value of c_j that meets the constraint on r_{KOZ}. The same can be done if c_j is set to zero, which instead results in $\phi_{c_{ij}} = \pi/2$. Notably, when a null c_i is considered, the initial conditions for the mth component of the motion associated with this mode can be computed from Eq. (48) by considering the known trigonometric identity $\sin(\text{atan}(x)) = x/\sqrt{x^2+1}$; a similar result is obtained by considering the identity $\cos(\text{atan}(x)) = 1/\sqrt{x^2+1}$ if a null c_j is considered. The two results are summarized in Eq. (51):

$$r_{\text{KOZ}} = \sqrt{c_i^2 + c_j^2}\, m_{ij,\min}(c_i, c_j)$$
$$m_{ij,\min}(c_i, c_j) = \min_{t\in[t_0, t_o+\tau_f]} \sqrt{\left(\boldsymbol{p}_{r,1}^T \boldsymbol{s}_{ij}(t)\right)^2 + \left(\boldsymbol{p}_{r,2}^T(t)\boldsymbol{s}_{ij}(t)\right)^2 + \left(\boldsymbol{p}_{r,3}^T(t)\boldsymbol{s}_{ij}(t)\right)^2} \tag{50}$$

$$x_{ij,m}(t_0) = c_j s_{ij,m}(t_0) = \begin{cases} c_j v_{j,m} & \text{if } c_i = 0 \\ c_i v_{i,m} & \text{if } c_j = 0 \end{cases} \tag{51}$$

Similarly, a maximum target–chaser separation can be identified as per Eq. (52) and represents a spherical keep-in zone of radius $\rho_{\text{sup},ij} = r_{\text{KIZ}}$. The same observations reserved to Eq. (50) apply to Eq. (52) as well, and the latter may also be employed for relative motion design:

$$r_{\text{KIZ}} = \sqrt{c_i^2 + c_j^2}\, m_{ij,\max}(c_i, c_j)$$
$$m_{ij,\max}(c_i, c_j) = \max_{t\in[t_0, t_o+\tau_f]} \sqrt{\left(\boldsymbol{p}_{r,1}^T \boldsymbol{s}_{ij}(t)\right)^2 + \left(\boldsymbol{p}_{r,2}^T(t)\boldsymbol{s}_{ij}(t)\right)^2 + \left(\boldsymbol{p}_{r,3}^T(t)\boldsymbol{s}_{ij}(t)\right)^2} \tag{52}$$

In the case of a center mode approximating a trivial motion as considered in Sec. III.B, function $\boldsymbol{s}_{ij}$ of Eq. (48) is approximated with a constant vector because $\omega_i \approx 0$. As a result, the motion is once again periodic with period τ and the maximum and minimum values of the relative distance $\rho_{ij}(t)$ can be computed as per Eqs. (49–52) but over a single period τ of the orbit of the target spacecraft. Therefore, the same considerations related to the design of a quasi-periodic motion using the center modes can be applied in this case as well.

IV. Applications to Relative Motion Design and Path Planning

This section examines how accurately the model based on fundamental modal solutions represents the system, and it explores its use for guidance and path planning. Specifically, the nonlinear and linearized relative motion equations derived in Sec. II and the model derived from the fundamental modal solution method according to the methodology of Sec. III are first tested to verify the accuracy with which they can model relative dynamics. Subsequently, the set of modal solutions is used to analyze the fundamental components of the relative motion in the velocity frame and characterize them from a geometrical standpoint. Finally, the modal decomposition representation is employed to compute target conditions for a path-planning strategy to approach a target object. All analyses are conducted considering a target spacecraft located on a nearly stable halo orbit around the L2 point, the initial conditions of which are reported in dimensionless Cartesian coordinates in Table 1. An L2 halo orbit is chosen for investigation due to the relevance of this region in the future development of cislunar operations [9,10,13,21]. The gravitational parameters ratio for the Earth–Moon system is taken as $\mu = 1.215058560962404 \times 10^{-2}$, whereas the reference values used to convert dimensionless quantities back to dimensional are taken as $\overline{r}_{em} = 3.89703 \times 10^8$ m and $\overline{\omega}_{\text{mi}} = 2.61110 \times 10^{-6}$ rad/s . The values of μ, $\overline{r}_{em}$, and $\overline{\omega}_{\text{mi}}$ are retrieved from the NASA Jet Propulsion Laboratory's Three-Body Periodic Orbits Catalog[¶].

Table 1 Dimensionless initial conditions of the L2 halo orbit of the target spacecraft

Reference frame	Initial state vector, $\boldsymbol{r}$
Synodal	$[1.08296, 0, 2.02317, 0, -2.01026, 0]^T$
MRF	$[-0.095106, 0, 0.202317, 0, 0.201026]^T$

Table 2 Eigenvectors and eigenvalues of state matrix Λ of the equivalent LTI system

Mode	Eigenvalue	Eigenvector
1	7.317×10^{-2}	$[-2.269 \times 10^{-2}, 0.998, -5.295 \times 10^{-2}, -5.660 \times 10^{-3}, -4.478 \times 10^{-2}, -2.563 \times 10^{-2}]^T$
2	$-i0.971$	$[1.023 \times 10^{-13}, 0.851, 1.124 \times 10^{-12}, 1.383, 1.006 \times 10^{-12}, -0.593]^T$
3	$-i0.971$	$[-0.143, 8.746 \times 10^{-13}, 0.315, 0, 0.945, 4.574 \times 10^{-13}]^T$
4	-2.477×10^{-10}	$[1.527 \times 10^{-10}, 2.000, 3.591 \times 10^{-10}, 1.514 \times 10^{-10}, 3.229 \times 10^{-11}, 6.923 \times 10^{-11}]^T$
	$-i8.486 \times 10^{-6}$	
5	-2.477×10^{-10}	$[-5.228 \times 10^{-6}, 0, -1.229 \times 10^{-5}, 8.867 \times 10^{-15}, -1.103 \times 10^{-6}, 4.033 \times 10^{-15}]^T$
	$+i8.486 \times 10^{-6}$	
6	-7.317×10^{-2}	$[2.269 \times 10^{-2}, 0.998, 5.295 \times 10^{-2}, -5.660 \times 10^{-3}, 4.478 \times 10^{-2}, -2.563 \times 10^{-2}]^T$

A. Application of the Method of Fundamental Modal Solutions

To apply the methodology discussed in Sec. III, Eq. (27) is first numerically integrated together with Eqs. (2) and (29) over a full target orbit period τ, representing the angular velocity and acceleration terms as per Eqs. (8), (9), (24), and (25) and the jerk term as per Eq. (26). The STM resulting from the final step of numerical integration is the monodromy matrix M of the system, from which Λ and the corresponding eigenvalues and eigenvectors can be computed as per Eqs. (33) and (35). Matrix $P(t)$ is then evaluated over one period and interpolated for use across multiple periods; this allows reducing the computational effort associated with the propagation at the cost of introducing errors if the system is not exactly periodic. The eigenvalues of Λ are reported in Table 2, showing that a relative motion occurring with respect to a target spacecraft starting from the initial conditions of Table 1 features a stable mode, an unstable mode, and four center modes. Of the latter modes, two have a null real part and the other two feature a negligible real part and an imaginary part on the order of 10^{-5}. This pair of conjugate eigenvalues with magnitude close to zero is due to the reference L2 orbit being not perfectly periodic, and therefore the two modes cannot be treated as a trivial pair without introducing an error. However, treating them as center modes allows correct modeling of the motion and the ability to deal with its slightly nonperiodic behavior. Applying the refactorization suggested in Sec. III.B, the fundamental solutions shown in Eq. (53) can be considered, in

[¶]Three-body Periodic Orbits–NASA Jet Propulsion Laboratory, California Institute of Technology. Available online at: https://ssd.jpl.nasa.gov/tools/periodic_orbits.html#/periodic [retrieved 17 May 2024].

which the change in nomenclature shown in Eq. (54) is applied for conciseness:

$$\begin{aligned} z_1(t) &= c_1 \boldsymbol{v}_1 e^{\lambda_1 (t-t_0)},\ \lambda_1 \in R, \lambda_1 > 0 \\ z_2(t) &= c_2[\boldsymbol{v}_2 \cos(\omega_2(t-t_0)) - \boldsymbol{v}_3 \sin(\omega_2(t-t_0))] \\ z_3(t) &= c_3[\boldsymbol{v}_2 \sin(\omega_2(t-t_0)) + \boldsymbol{v}_3 \cos(\omega_2(t-t_0))] \\ z_4(t) &= c_4[\boldsymbol{v}_4 \cos(\omega_4(t-t_0)) - \boldsymbol{v}_5 \sin(\omega_4(t-t_0))] \\ z_5(t) &= c_5[\boldsymbol{v}_4 \sin(\omega_4(t-t_0)) + \boldsymbol{v}_5 \cos(\omega_4(t-t_0))] \\ z_6(t) &= c_6 \boldsymbol{v}_6 e^{\lambda_6 (t-t_0)},\ \lambda_6 \in R,\ \lambda_6 < 0 \end{aligned} \tag{53}$$

$$\begin{aligned} &\omega_2 = |\text{imag}(\lambda_2)| = |\text{imag}(\lambda_3)|, \quad \omega_4 = |\text{imag}(\lambda_4)| = |\text{imag}(\lambda_5)| \\ &\boldsymbol{c} = [c_1,\ c_2,\ c_3,\ c_4,\ c_5,\ c_6]^T = [c_1,\ c_{R1},\ c_{I1},\ c_{R2},\ c_{I2},\ c_6]^T \\ &V = [\boldsymbol{v}_1,\ \boldsymbol{v}_2,\ \boldsymbol{v}_3,\ \boldsymbol{v}_4,\ \boldsymbol{v}_5,\ \boldsymbol{v}_6] \\ &\quad = [\boldsymbol{v}_1,\ 2\boldsymbol{v}_{R1},\ -2\boldsymbol{v}_{I1},\ 2\boldsymbol{v}_{R2},\ -2\boldsymbol{v}_{I2},\ \boldsymbol{v}_6] \end{aligned} \tag{54}$$

For completeness, Table 2 also shows the eigenvectors associated with Λ as already refactored according to Eq. (53). The refactorization drastically reduces the magnitude of $\boldsymbol{v}_5$, whose components are of the same order of magnitude of the corresponding eigenvalue. On the other hand, the second component of $\boldsymbol{v}_4$ is the largest of the set, whereas all other components are negligible. In addition, because ω_4 is on the order of 10^{-5}, the period of the oscillations described in $z_4(t)$ and $z_5(t)$ in Eq. (53) is on the order of 10^5. Therefore, from a geometrical perspective, the term resulting from $z_4(t) + z_5(t)$ is the composition of an offset approximately oriented along the velocity axis and a linear drift superimposed to an oscillation with period τ; modes 4 and 5 thus represent a center mode approximating a trivial motion. This model is coherent with the fact that if the chaser shares the same orbit of the target at the initial time (i.e., only the fourth coefficient of the set has a nonzero value), the two spacecraft are initially separated in the velocity direction only, and the chaser oscillates along this direction as time passes. If a positive fifth coefficient is introduced, this results in a small vertical negative position offset due to the first component of vector $\boldsymbol{v}_5$, resulting in a drift along the negative flight-path direction as the negative sign of the fifth component of $\boldsymbol{v}_5$ shows, to which an oscillation with period τ due to $P(t)$ is superimposed.

B. Modeling Accuracy Assessment

To compare the previously described models and assess their accuracy, a solution is first computed by numerically propagating the target and chaser orbits separately through the CR3BP equations for 10 orbital periods (i.e., 105.65 days). Then, the same motion is propagated using the nonlinear and linearized equations of relative motion provided by Eqs. (7) and (10), respectively, as well as using the solution found through the method of fundamental modal solutions shown in Eq. (35). The different solutions are compared by evaluating the errors on the Cartesian relative position and velocity expressed and observed in the VRF and according to Eq. (55), where subscript "r" identifies the reference solution:

$$\begin{aligned} e_x &= x - x_r, & e_y &= y - y_r, & e_z &= z - z_r, \\ e_{\dot{x}} &= \dot{x} - \dot{x}_r, & e_{\dot{y}} &= \dot{y} - \dot{y}_r, & e_{\dot{z}} &= \dot{z} - \dot{z}_r \end{aligned} \tag{55}$$

A representation of the natural, nonforced relative motion starting from the arbitrary initial conditions given by the set of coefficients $\boldsymbol{c} = [5\times10^{-7}, 2\times10^{-6}, 2\times10^{-6}, 5\times10^{-7}, 1\times10^{-7}, 5\times10^{-7}]^T$ is shown in Fig. 2, where the motion propagated using all previously stated models is shown, whereas Fig. 3 shows the temporal evolution of the components of the Cartesian state vector. In addition, the errors of the modal, linear, and nonlinear models compared with the numerically integrated motion in the CR3BP are shown in Fig. 4. The diagrams show that although all models agree with the numerical propagation in terms of magnitude of the observed dynamics, they achieve different levels of accuracy. Specifically, the nonlinear model shows a negligible error (i.e., on the order of millimeters in position and 10^{-8} m/s in velocity) with respect to the numerical propagation, due to the two solutions being mathematically equivalent. Similarly, the modal decomposition solution shows good agreement with the linearized one, with errors on the order of

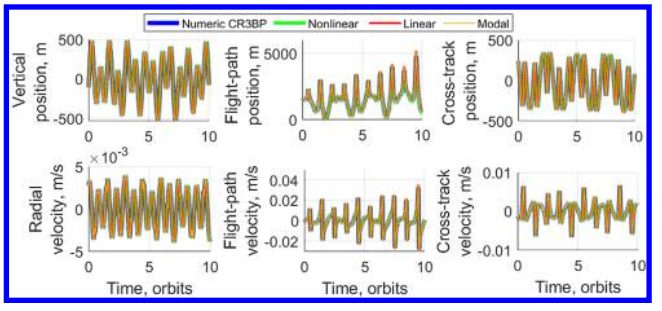

Fig. 3 Cartesian state vector components of relative motion propagated with the considered models.

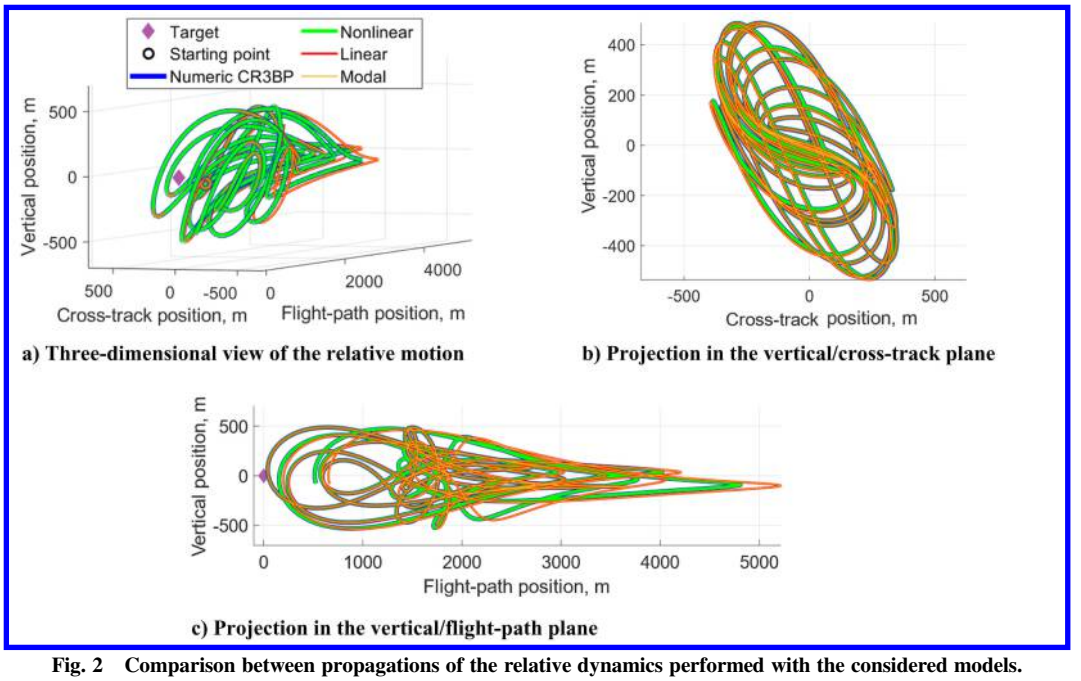

Fig. 2 Comparison between propagations of the relative dynamics performed with the considered models.

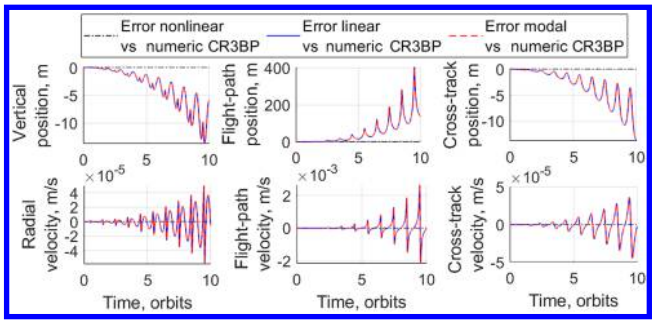

Fig. 4 Errors on components of the Cartesian representation of the propagated relative state.

Table 3 Comparison between nonlinear and modal decomposition solutions against CR3BP equations numerical integration

Error on norm of relative state vectors	Nonlinear model		Modal decomposition model	
	Position, m	Velocity, m/s	Position, m	Velocity, m/s
Mean	9.20×10^{-4}	2.75×10^{-9}	51.21	1.53×10^{-4}
Standard deviation	1.34×10^{-3}	6.55×10^{-9}	69.27	3.45×10^{-4}
Maximum	7.95×10^{-3}	5.27×10^{-8}	403.84	2.64×10^{-3}
Minimum	-1.09×10^{-5}	-2.81×10^{-9}	−0.21	-1.26×10^{-4}

10^{-6} m in position and 10^{-10} m/s in velocity, because the modal decomposition model is derived from the linearized equations of motion. On the other hand, a comparison of the modal decomposition and linearized solutions against the numerical integration of the dynamics highlights errors that are at least two orders of magnitudes smaller than the magnitude of the relative state after five orbital periods while raising up to one-tenth of this magnitude after 10 orbital periods. Notably, an oscillatory trend is superimposed to this growth in magnitude; this is a linearization error associated with the nonperfect periodicity of the considered orbit.

Statistics are shown in Table 3 concerning the comparisons of the norms of the relative position and velocity vectors propagated by the nonlinear and modal decomposition models against the numerical integration of the CR3BP equations, confirming the observed results. This analysis thus shows that the considered linearized model and equivalently its modal decomposition representation can be used to describe the relative motion with errors at least two orders of magnitude smaller than the relative state itself for multiple orbit periods. To retain such accuracy over time, the linearization requires to be recomputed periodically.

To provide further insight into the relative dynamics, Fig. 5 shows the three-dimensional evolution of the single modes of motion, computed according to Eq. (53). In Fig. 5a, modes 1 and 6 evidently represent the drifting behavior and initial offset with respect to the flight-path axis, with oscillations along all directions that are periodic with period τ due to matrix $P(t)$, with the largest one along the flight-path direction. The direction of oscillation is related to the nonzero terms (i.e., components 1 to 3) of eigenvectors $\boldsymbol{v}_1$ and $\boldsymbol{v}_6$, as shown in Table 2, with the second one being the largest. Modes 2 and 3 shown in Fig. 5b coherently represent a bounded quasi-periodic motion around the target, whose quasi periodicity is due to the incommensurability between the LTI description of the solution, periodic with period $2\pi/\omega_2$, and $P(t)$, periodic with period τ. Concerning the modes approximating the trivial motion, Fig. 5c shows that mode 4 translates into a bounded periodic motion, representing the offset portion of the trivial mode, and Fig. 5d coherently represents the drifting term, as highlighted by the along-track position component showing a drifting trend superimposed to the periodic oscillations. In both modes 4 and 5, the latter oscillations are specifically due to the periodic effect of $P(t)$.

C. Relative Motion Design Under Geometrical Constraints

The modal decomposition of relative motion obtained in Sec. IV.A is now applied to the design of simple trajectories using modal coefficients as ROEs. A representative case is considered for each characteristic motion based on the geometrical interpretations given in Sec. III.B to illustrate how efficient relative motion design can be achieved for different mission objectives. These examples also prove that combining geometric parameters with modal coefficients enables direct exploitation of the manifolds inherent to the CR3BP framework, allowing for propellantless relative maneuvers for approach and departure, inspection, and loitering. In the following, each motion is propagated by both using the modal decomposition

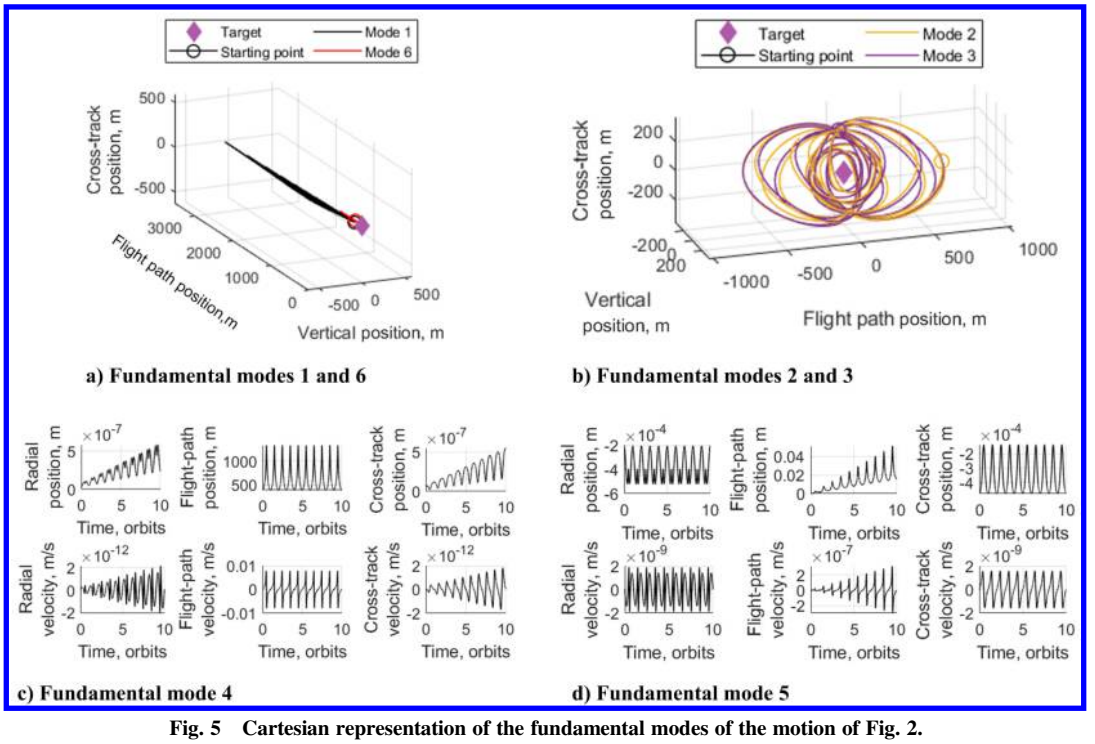

Fig. 5 Cartesian representation of the fundamental modes of the motion of Fig. 2.

model and numerically integrating the CR3BP equations of the absolute dynamics of the target and chaser spacecraft.

1. *Drifting Motion Toward the Target*

The following case exemplifies the use of the coefficients of the stable mode to design a natural drifting motion occurring approximately along the flight-path axis and approaching the target object from the negative flight-path direction, such that the arrival point is at a separation $\overline{\rho}_{\text{des}}$ of 20 m from the target. Considering the periodicity of the stable mode due to the presence of matrix $P(t)$, a local minima of the target–chaser separation function $\rho_i(t)$ can be exploited as the target state of the approach. Imposing $\rho_{\text{inf}}, i(tf) = \rho_{\text{des}} = \overline{\rho}_{\text{des}}/r_{em}$, Eq. (46) can be inverted to obtain Eq. (56) and evaluate coefficient c_6 based on the imposed geometrical constraint; then, Eq. (57) can be solved numerically to find the value of t_f that simultaneously satisfies Eqs. (56) and (57). The sign of the coefficient is chosen to be negative to conduct the approach from the negative flight-path direction, based on the sign of the elements of the eigenvector of the stable mode. This design problem is solved by considering the initial conditions at $t_0 = 0.5\tau$ to exploit the periodicity of the motion so that the chaser initial velocity vector is already directed toward the target spacecraft. The initial conditions of the absolute dynamics of the target spacecraft at t_0, required for trajectory design and for the numerical propagation of motion, are obtained by propagating the motion of the target from the conditions in Table 1 for half an orbit period:

$$|c_i(t_f)| = \rho_{\text{des}}/(d_{\rho,m}e^{\lambda_i t_f}) \tag{56}$$

$$\rho_i(t_f) = |c_i(t_f)|\left(\sqrt{(\boldsymbol{p}_{r,1}^T(t_f)\boldsymbol{\alpha})^2 + (\boldsymbol{p}_{r,2}^T(t_f)\boldsymbol{\alpha})^2 + (\boldsymbol{p}_{r,3}^T(t_f)\boldsymbol{\alpha})^2}\right)e^{\lambda_i t_f} \tag{57}$$

The solution of Eqs. (56) and (57) results in $c_6 = -1.9566 \times 10^{-7}$ with all other coefficients equal to zero and $t_f = 0.979\tau$, i.e., 10.34 days, which is coherently close to a full period of the orbit where the next minimum of the function $\rho_i(t)$ is expected. The motion is represented in Fig. 6a in terms of the Cartesian components of the state vector, also including the inferior and superior limits for each component computed through Eqs. (44) and (45). Moreover, Fig. 6b shows the evolution of the target–chaser separation together with the inferior and superior limits $\rho_{\text{inf},i}(t)$ and $\rho_{\text{sup},i}(t)$, computed through Eqs. (46) and (47). The diagrams show that the chaser successfully coasts toward the target along an approach direction that is almost parallel to the flight-path axis, differing from the latter due to the properties of the stable manifold, and correctly reaches the desired target condition. Notably, the minimum desired separation of 20 m is not overcome during the approach, as shown by Fig. 6b, where the motion is propagated for a further 0.2 orbits to show that the constraint is satisfied. Overall, Fig. 6 highlights the good agreement between the modal decomposition approach and the motion propagated using the CR3BP equations, as well as between the mathematical representation of geometrical properties described in Eqs. (44–47) and the actual motion. Specifically, the largest error between the modal decomposition representation and the numerical integration of the CR3BP equations is expectedly obtained at the end of the propagation, with millimeter-level error on the relative position and errors on the order of 10^{-8} m/s on the norm of the relative velocity vector. A similar approach to the one considered in this section can also be considered when dealing with the design of a drifting motion departing from the target spacecraft using the unstable mode.

2. *Quasi-Periodic Motion Around the Target*

The second case under consideration uses the center modes of the motion to design a quasi-periodic trajectory around the target with a keep-out sphere of radius $\overline{r}_{\text{KOZ}} = 30$ m. This type of motion is particularly useful to perform loitering and inspection maneuvers around the target object, given that the variations in target–chaser distance and the quasi-periodicity of the motion do not affect operations [13]. Because no specific constraint is imposed on the initial conditions of the motion, c_2 is imposed to be zero, c_3 is computed according to Eq. (50) considering $r_{\text{KOZ}} = \overline{r}_{\text{KOZ}}/r_{em}$, and c_3 is taken positive without loss of generality; therefore, for $t_0 = 0$, coefficient c_3 is set to 5.3257×10^{-7} and all other coefficients are set to zero. The resulting motion is shown in three dimensions in Fig. 7a and in terms of the target–chaser separation in in Fig. 7b, where the superior and inferior limits are computed according to Eqs. (50) and (52). The graphs show that the designed trajectory effectively stays out of the desired spherical keep-out zone and the models estimating superior and inferior limits can accurately describe the bounds of the dynamics. Because slight violations of the these bounds can occur due to the approximation on τ_f considered in Eq. (49), applying a safety margin on the required r_{KOZ} can prevent unwanted violations of the keep-out zone. Moreover, Fig. 7 further highlights the agreement between the motions propagated using the modal decomposition model and the CR3BP equation. Specifically, the maximum errors between the modal decomposition representation and the numerical integration of the CR3BP equations are coherently achieved at the end of the propagation and are on the orders of centimeters for the relative position and of 10^{-8} m/s for the relative velocity.

3. *Bounded Motion Along the Flight-Path Direction*

If the chaser spacecraft is required to hold a specific position during operations, the dynamics of the CR3BP require that a continuous control profile is employed even if the chaser shares the same orbit of the target. However, when a bounded motion suffices instead, the center modes approximating the trivial motion can be employed to achieve a bounded motion along the flight-path direction. A design example is provided in the following by considering a minimum target–chaser separation of 50 m as a design constraint. In this respect, Table 2 shows that $\boldsymbol{v}_4$ has only the second component as substantially different from zero at $t_0 = 0$, whereas all components of $\boldsymbol{v}_5$ approach zero. Therefore, imposing $c_5 = 0$, Eq. (50) is used to assess that the desired value of c_4 is 6.4151×10^{-8}, whereas all other coefficients can be set to zero.

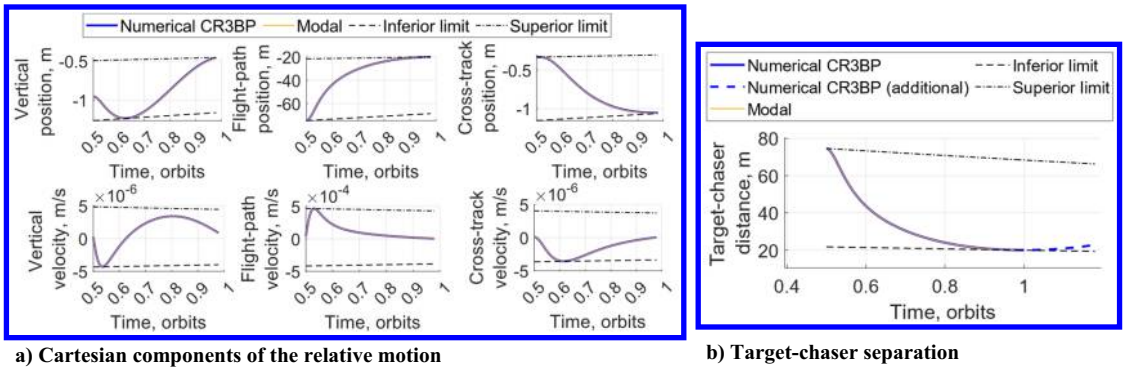

a) Cartesian components of the relative motion **b) Target-chaser separation**

Fig. 6 Natural drifting motion toward the target, designed using the stable mode.

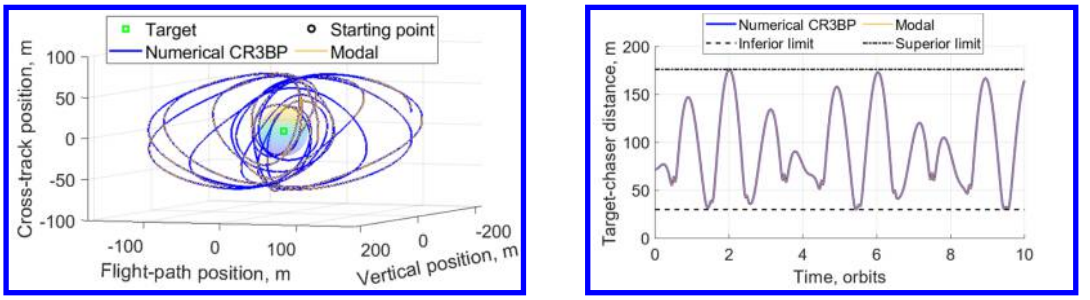

a) Three-dimensional view with representation of the keep-out sphere

b) Target-chaser separation

Fig. 7 Quasi-periodic motion for target in section with a keep-out sphere of 30 m.

As for the sign of c_4, eigenvalue $\boldsymbol{v}_4$ shows that a positive coefficient allows placing the chaser in a leading position with respect to the target. The propagated motion is shown in Fig. 8 in terms of the target–chaser separation and the single components of the Cartesian state vector; specifically, Fig. 8a shows that the motion is effectively bounded and always stays above the desired target–chaser separation. As in the previous case, the superior and inferior limits of the motion are computed using Eqs. (50) and (52). Whereas the modal propagation of the motion is expectedly contained within the prescribed bounds at any time, the numerical propagation of the motion through the CR3BP equations begins to slightly violate the boundaries after 10 orbital periods (i.e., 105.65 days). This is due to the error buildup of the modal decomposition propagation, which is evident from Fig. 8b and amounts to a few centimeters and to less than hundredths of millimeters per second after 10 orbits.

D. Modal Coefficients as Relative Orbital Elements for Path Planning

Because each set of coefficients of modal decomposition represents a different relative trajectory, they can be used as ROEs to design an approach transfer for the chaser spacecraft to get in proximity of the target. In the following, an example of this application is provided using impulsive control. The approach maneuver is split into multiple transfers and the intermediate states can be designed to satisfy desired constraints (e.g., safety or operational constraints involving minimum target–chaser separations) by selecting the appropriate values of the coefficients. The Δvs of the impulsive maneuvers are evaluated by applying a state-of-the-art method proposed by Guffanti and D'Amico [38] to compute fuel-efficient maneuvers, which has been reformulated in this work to employ vector $\boldsymbol{c}$ as the set of ROEs. Considering a predetermined duration of the transfer from an initial state $\boldsymbol{c}_0$ to a desired state $\boldsymbol{c}_{\text{des}}$, the method computes the number of required Δvs to accomplish the transfer, the times of applications of the impulsive Δvs, and the corresponding magnitudes and directions. During the approach, the accuracy at the arrival state of each transfer is evaluated by comparing the achieved and desired sets of coefficients $\boldsymbol{c}_i^*$ and $\boldsymbol{c}_i$, as well the corresponding Cartesian representation of the relative states. The total cost of the approach is evaluated by adding up the Δvs required for each transfer, which is computed as the norm of the vector representing the increment of velocity.

1. *Impulsive Burns Computation Method*

In their work, Guffanti and D'Amico [38] highlighted that a relative motion can be decomposed in an osculating term $\boldsymbol{f}'(\boldsymbol{x},t)$, a perturbing term $\boldsymbol{f}_p(\boldsymbol{x},t)$, and a control term, according to Eq. (58). Defining $\boldsymbol{\kappa}$ as a set of constants of integration of the motion and considering that the osculating motion $\partial\boldsymbol{x}/\partial t = \boldsymbol{f}'(\boldsymbol{x},t)$ corresponds to a single set $\boldsymbol{\kappa}$, the relative dynamics of Eq. (58) can equivalently be represented using the integration constants variational equation reported in Eq. (59), where $\partial\boldsymbol{\kappa}/\partial\boldsymbol{x}$ is the Jacobian matrix of the mapping function between the constants of integration $\boldsymbol{\kappa}$ and the Cartesian relative state $\boldsymbol{x}$:

$$\begin{aligned}\dot{\boldsymbol{x}}(t) &= \boldsymbol{f}'(\boldsymbol{x},t) + \boldsymbol{f}_p(\boldsymbol{x},t) + B(t)\boldsymbol{u}(t)\\ &= \frac{\partial\boldsymbol{x}(\boldsymbol{\kappa},t)}{\partial t} + \frac{\partial\boldsymbol{x}(\boldsymbol{\kappa},t)}{\partial\boldsymbol{\kappa}}\frac{\partial\boldsymbol{\kappa}}{\partial t} + B(t)\boldsymbol{u}(t)\end{aligned} \tag{58}$$

$$\dot{\boldsymbol{\kappa}} = \frac{\partial\boldsymbol{\kappa}}{\partial\boldsymbol{x}(\boldsymbol{\kappa},t)}\boldsymbol{f}_p(\boldsymbol{x},t) + \frac{\partial\boldsymbol{\kappa}}{\partial\boldsymbol{x}(\boldsymbol{\kappa},t)}B(t)\boldsymbol{u}(t) \tag{59}$$

Reformulating Eq. (59) using the coefficients of the modal decomposition as constants of integration, Eq. (36) results in $\partial\boldsymbol{c}/\partial\boldsymbol{x} = \Psi^{-1}(t)$. The perturbing term $\boldsymbol{f}_p(\boldsymbol{x},t)$ is neglected because perturbing actions are not considered in this work. The formulation proposed in [38] can then be employed to solve the optimization problem reported in Eq. (60) and obtain the directions of the optimal impulsive burns $\Delta\hat{\boldsymbol{v}}(t_i) = B_c^T(t_i)\boldsymbol{\eta}$ as those that satisfy the condition $\|B_c^T(t_i)\boldsymbol{\eta}\| = 1$ at times t_i, considering $B_c(t_i) = \Psi^{-1}(t)B$. The magnitudes of the burns required to achieve the variation $\Delta\boldsymbol{c}_{\text{des}} = \boldsymbol{c}_{\text{des}} - \boldsymbol{c}_0$ can be obtained by solving the system of linear equations shown in Eq. (61). As also observed in [38], usually the condition $\|B_c^T(t_i)\boldsymbol{\eta}\| = 1$ is not satisfied perfectly and requires considering a tolerance that can be selected as arbitrarily small. In general, larger tolerance values allow identification of more variegate transfer solutions at the cost of higher Δvs:

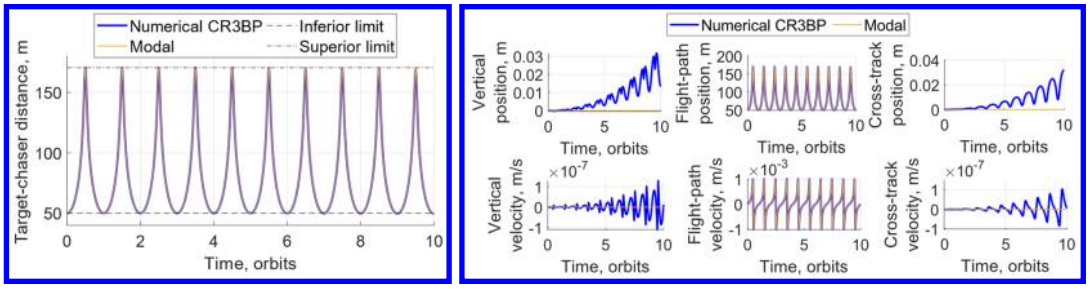

a) Target-chaser separation

b) Cartesian components of the relative motion

Fig. 8 Bounded motion along flight-path direction with minimum target–chaser separation of 50 m.

$$\underset{\underline{\eta}}{\text{maximize}}\ J_d = \boldsymbol{\eta}^T \Delta \boldsymbol{c}_{\text{des}} \quad \text{subject to } \|B_c^T(t_i)\boldsymbol{\eta}\| \le 1, \quad t_j \in [t_0, t_f] \tag{60}$$

$$[\ldots\ B_c(t_i)\Delta\hat{\boldsymbol{v}}(t_i)\ \ldots] \begin{bmatrix} \vdots \\ \|\Delta \boldsymbol{v}(t_i)\| \\ \vdots \end{bmatrix} = \Delta \boldsymbol{c}_{\text{des}} \tag{61}$$

2. Approach Maneuver Sequence

The approach sequence considered in the following is articulated in three phases. The first phase begins at $t_0 = 0$, with the chaser at 1 km of separation from the target object on the negative flight-path direction. After an initial waiting time of 0.005τ (i.e., about 1.27 h), the chaser performs three transfers to gradually approach the target along the negative flight-path axis, moving between bounded relative trajectories aligned along the flight-path direction and with desired minimum target–chaser distances of 500, 250, and 100 m, respectively. The three maneuvers are separated by waiting times of 0.005τ; once the third transfer is completed, the chaser further waits 0.005τ before resuming the operations. At this point, the second phase of the approach sequence begins, in which the chaser transfers onto a quasi-periodic relative trajectory to perform target inspection. The trajectory has a desired keep-out sphere of radius $\bar{r}_{\text{KOZ}}$ of 25 m and is centered in the target, allowing the chaser to effortlessly and safely coast while performing the inspection. After 5.05τ (i.e., about 53.35 days), the last phase of the approach begins, in which the chaser transfers onto a bounded relative trajectory that is once again aligned along the negative flight-path axis and features a desired minimum target–chaser separation of 25 m. An additional propagation of the motion is conducted for a full orbit of the target spacecraft after the maneuver has completed to verify that the desired final condition is met.

The sets of coefficients of the intermediate states constituting the approach sequence are summarized in Table 4 and are computed based on the methodology proposed in Sec. IV.C; the initial state $\boldsymbol{c}_0$ is the only one being computed from the corresponding Cartesian representation. Comparing states $\boldsymbol{c}_0$ and $\boldsymbol{c}_1$, $\boldsymbol{c}_2$, $\boldsymbol{c}_3$, and $\boldsymbol{c}_5$, they expectedly share the same form because the motion corresponding to the set $\boldsymbol{c}_0$ is also bounded along the flight-path axis. Notably, the possibility of evaluating how each Δv affects the coefficients of modal decomposition using Eq. (59) allows computation of all maneuvers in advance; these are summarized in Table 5 together with the segments of the approach sequence and the transfers. The duration of each transfer between two states is chosen to provide a feasible solution.

Table 4 Summary of the intermediate states of the chaser during the approach maneuver

State	Coefficients set	Description of corresponding state
$\boldsymbol{c}_0$	$[0, 0, 0, -1.283 \times 10^{-6}, 0, 0]$	Point at 1 km from target, on the negative flight-path direction
$\boldsymbol{c}_1$	$[0, 0, 0, -6.415 \times 10^{-7}, 0, 0]$	Bounded motion along the negative flight-path direction, with a minimum target–chaser separation of 500 m
$\boldsymbol{c}_2$	$[0, 0, 0, -3.208 \times 10^{-7}, 0, 0]$	Bounded motion along the negative flight-path direction, with a minimum target–chaser separation of 250 m
$\boldsymbol{c}_3$	$[0, 0, 0, -1.283 \times 10^{-7}, 0, 0]$	Bounded motion along the negative flight-path direction, with a minimum target–chaser separation of 100 m
$\boldsymbol{c}_4$	$[0, 0, -4.438 \times 10^{-7}, 0, 0, 0]$	Quasi-periodic motion around the target, with a keep-out sphere of radius 25 m centered in the target
$\boldsymbol{c}_5$	$[0, 0, 0, -3.208 \times 10^{-8}, 0, 0]$	Bounded motion along the negative flight-path direction, with a minimum target–chaser separation of 25 m

Table 5 Chaser approach strategy, with indication of transfers, times of flight, and Δvs

Phase	Approach segment: Identifier	Approach segment: Description	Initial time τ	Final time τ	Δv, cm/s
1	W1	Waiting	0	0.005	— —
	T1	Transfer from $\boldsymbol{c}_0$ to $\boldsymbol{c}_1$	0.005	0.105	1.134
	W2	Waiting	0.105	0.110	— —
	T2	Transfer from $\boldsymbol{c}_1$ to $\boldsymbol{c}_2$	0.110	0.210	0.587
	W3	Waiting	0.210	0.215	— —
	T3	Transfer from $\boldsymbol{c}_2$ to $\boldsymbol{c}_3$	0.215	0.515	0.278
	W4	Waiting	0.515	0.520	— —
2	T4	Transfer from $\boldsymbol{c}_3$ to $\boldsymbol{c}_4$	0.520	1.470	4.736×10^{-2}
	IS	Inspection	1.470	6.520	— —
3	T5	Transfer from $\boldsymbol{c}_4$ to $\boldsymbol{c}_5$	6.520	6.701	5.746×10^{-2}
	FP	Final propagation	6.701	7.701	— —

Overall, the approach maneuver requires 7.701τ (i.e., about 81.36 days) to complete and a total Δv of 2.104 cm/s. A three-dimensional representation of the relative state of the chaser with respect to the target during the approach is shown in Fig. 9; however, the approach trajectory can be analyzed in greater detail by observing each phase separately.

The first phase of the approach is illustrated in Fig. 10 in terms of both the temporal evolutions of the Cartesian state vector and the modal coefficients, and dashed black lines between asterisks represent discontinuities due to the application of a Δv. In this respect, Fig. 10a shows that a cost-effective solution for a transfer along the flight-path axis is that of a hop between the two points, coherently with other results observed in the literature [13]. Notably, the last hop requires a longer time to be executed because shorter times may lead to unfeasible solutions that do not allow reaching the desired state. Table 6 reports the values of the sets of coefficients that have been achieved at the end of each of the first three transfers as shown in Fig. 10b. Compared to the target values $\boldsymbol{c}_1$, $\boldsymbol{c}_2$ and $\boldsymbol{c}_3$ in Table 4, the sets achieved at the end of transfers T1, T2, and T3 all feature large errors on the first, fifth, and last coefficients of the set. Specifically, on transfer T1, the coefficients of the stable and unstable modes of the motion are almost equivalent in magnitude and opposite in sign, and they provide a drifting contribution toward the negative flight-path direction to the final natural motion. The situation changes for transfer T2, where the two modes contribute overall with a drift toward the positive flight-path direction, due to the sixth coefficient being the largest in magnitude; the same contribution can be observed for transfer T3, although it is related to the two coefficients being similar in magnitude and opposite in sign. During all three transfers, the fifth mode contributes with a drift term toward the negative flight-path direction. Overall, however, all the drifting contributions are negligible over the short waiting time that follows each maneuver. As a final remark, observing Fig. 10b, it is worth noting that the large values achieved by the fifth coefficient across the maneuvers are a direct consequence of the fact that the entries of eigenvector $\boldsymbol{v}_5$ are close to zero, thus requiring large values of the corresponding coefficient in order for this mode to affect the motion.

The second phase of the approach is illustrated in Fig. 11, showing that the transition from the oscillatory motion along the flight-path axis to the quasi-periodic inspection motion requires three impulses to occur, which are smaller than those that occurred in the first phase and on the order of 10ths of millimeters per second. This is in line with the slow dynamics that naturally characterize the CR3BP; for these maneuvers to take place and leverage the achieved natural relative motion, propulsive units are thus required to be capable of providing Δvs below the millimeter-per-second level.

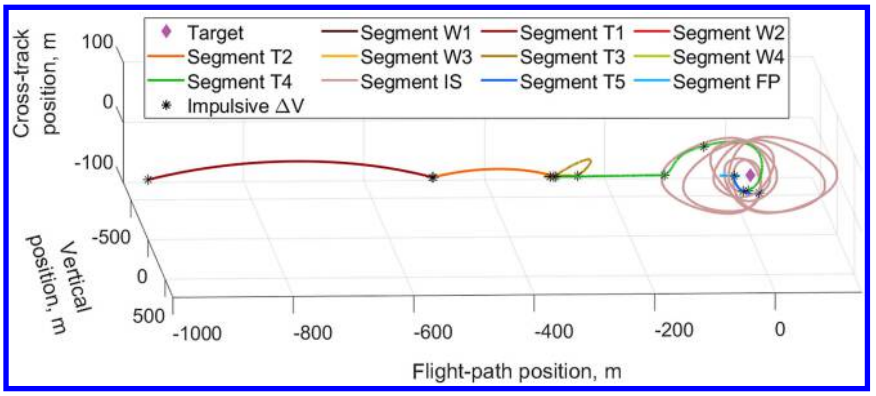

Fig. 9 Three-dimensional view of the approach trajectory.

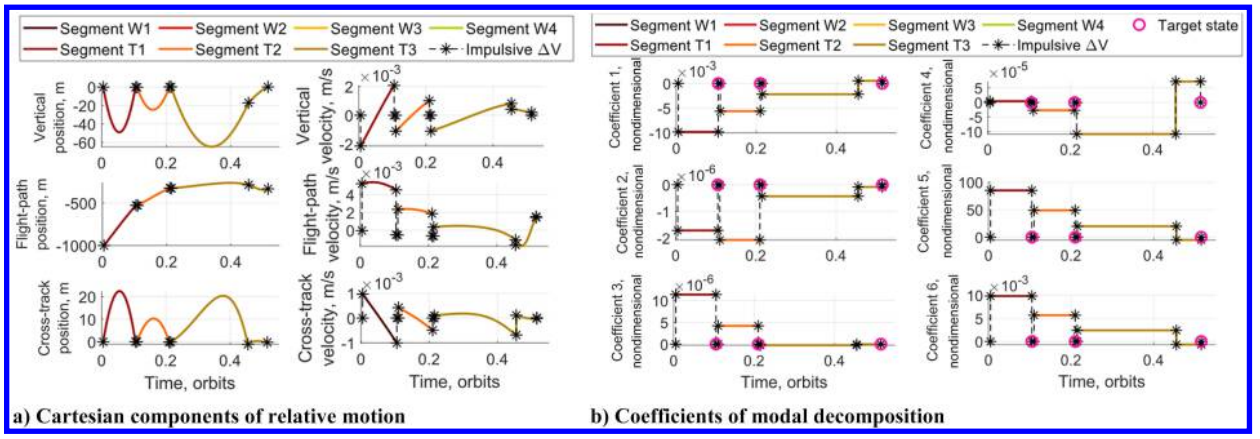

Fig. 10 Cartesian state vector and modal coefficients during phase 1 of the approach.

Table 6 Achieved states c_1^*, c_2^*, and c_3^* for phase 1 of the approach

Transfer segment	Achieved state, represented through modal coefficients
T1	$[-1.176\times10^{-8}, -5.515\times10^{-9}, -8.542\times10^{-9}, -6.421\times10^{-7}, -3.853\times10^{-5}, 1.274\times10^{-8}]$
T2	$[-8.915\times10^{-9}, 1.408\times10^{-9}, 5.221\times10^{-10}, -3.229\times10^{-7}, -8.928\times10^{-5}, -3.154\times10^{-8}]$
T3	$[5.121\times10^{-7}, -4.933\times10^{-9}, 5.889\times10^{-9}, -7.284\times10^{-8}, -4.876\times10^{-3}, -6.242\times10^{-7}]$

The set of coefficients achieved at the end of transfer T4 is $c_4^* = [2.496\times10^{-8}, -3.838\times10^{-9}, -4.435\times10^{-7}, 2.642\times10^{-9}, -2.990\times10^{-4}, -3.177\times10^{-8}]^T$, showing that the largest error affects the coefficients of the drifting modes and the fifth coefficient, associated with the drift term of the trivial motion. Specifically, the error on the coefficient of the unstable mode is negative and larger in magnitude than the one on the coefficient of the stable mode, and the fifth coefficient is negative and four orders of magnitude larger than the other two. As a result, these three drifting contributions approximately balance each other over the considered time interval, and the center of the quasi-periodic trajectory oscillates around the target. The smallest target–chaser separation achieved during the motion amounts to 20.43 m.

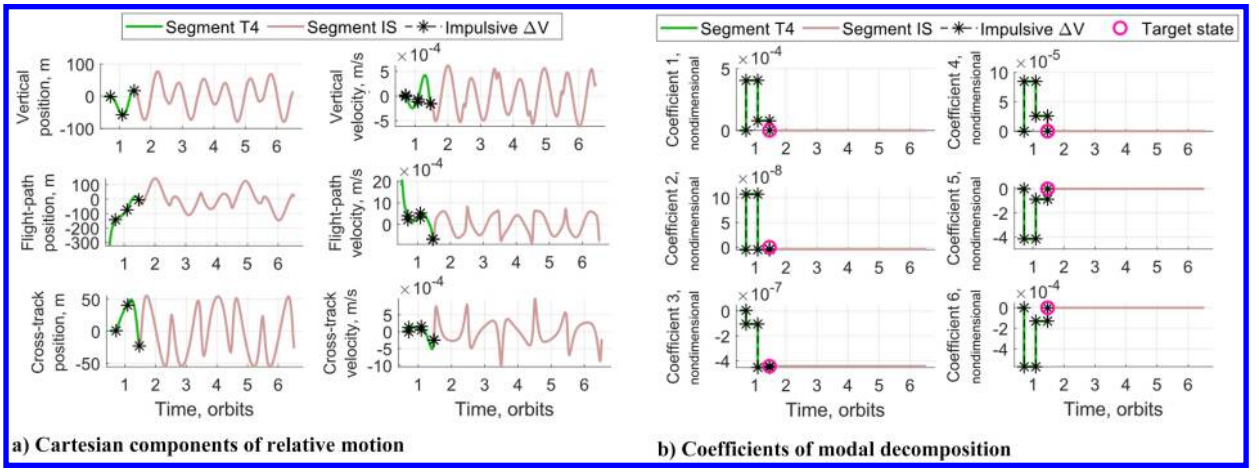

Fig. 11 Cartesian state vector and modal coefficients during phase 2 of the approach.

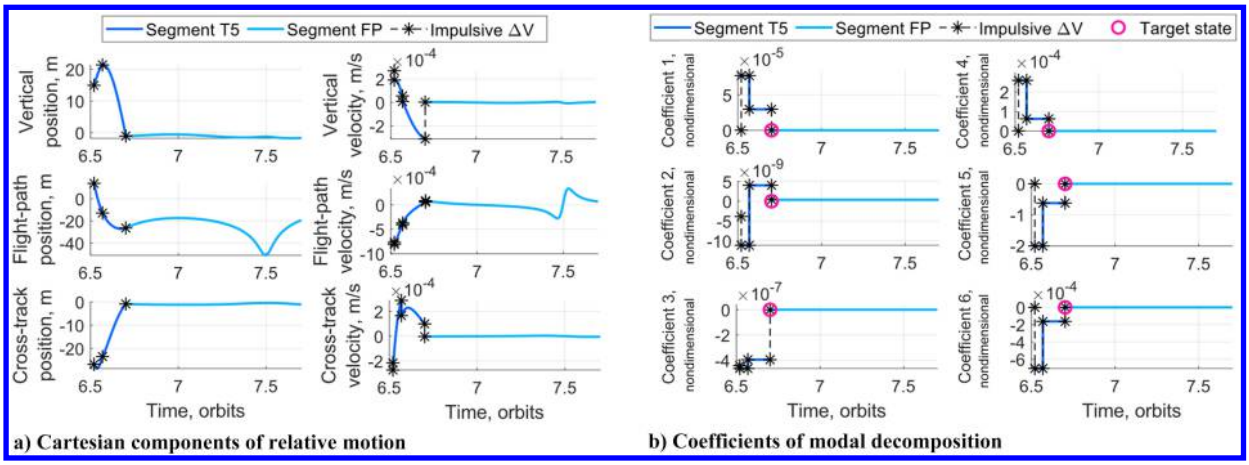

Fig. 12 Cartesian state vector and modal coefficients during phase 3 of the approach.

The third and last phase of the approach is illustrated in Fig. 12 and includes the final motion propagation after the last maneuver. The figure shows that three impulsive burns are required to maneuver from the quasi-periodic trajectory back to the flight-path axis, and the magnitude of the impulsive Δvs is comparable to that observed in the previous case, as shown in Table 5. The final state achieved at the end of the transfer is $c_5^* = [3.574 \times 10^{-8}, 3.905 \times 10^{-10}, -4.140 \times 10^{-10}, -3.378 \times 10^{-8}, -3.051 \times 10^{-4}, -3.901 \times 10^{-8}]^T$, once again showing that the three largest errors in achieving the final state occur on the first, fifth, and sixth coefficients of the set, and the same considerations of the previous case apply. In fact, the positive sign of the coefficient of the unstable motion would imply a drift away from the target from a point in front of the latter; on the contrary, the negative sign of the sixth coefficient would result in a drift toward the target from a trailing point behind the latter. The motion resulting from only the first and last coefficients would produce a drift away from the target in the positive flight-path direction. However, adding the trivial mode, governed by the fourth and fifth coefficients, minimizes this drift over a single orbit, leading to a closest target–chaser separation of 17.43 m at the end of the approach.

V. Conclusions

This paper presents a set of equations of relative motion in the context of the circular restricted three-body problem (CR3BP) and an application of the method of fundamental modal solutions to these equations to gain geometrical insight in the motion for trajectory design and path planning. A target-fixed velocity-based orbiting reference frame is chosen for the derivation of the equations of relative motion. The frame is centered in the target spacecraft and considers the instantaneous velocity direction as one of the fundamental directions of the frame, thus allowing a more intuitive representation of the relative dynamics as opposed to other choices of orbiting frames. The method of the fundamental modal solutions is then applied to describe a general solution as a weighted sum of the fundamental components (that is, the modes) of the motion. The paper shows that the coefficients of this weighted sum, known as coefficients of modal decomposition, and the eigenvalues and eigenvectors of the corresponding fundamental modes can be effectively used to design relative trajectories that can satisfy specific geometric constraints. In this respect, mathematical relations are proposed to model important geometrical properties of the motion and relate them to the coefficients of modal decomposition. Moreover, design examples are proposed involving periodic, quasi-periodic, and drifting motion for a target spacecraft on an L2 halo orbit. Finally, the paper shows that the coefficients of modal decomposition can also be effectively employed as relative orbital elements for the formulation of guidance and control solutions. To this purpose, an example is provided in which an approach trajectory is planned with multiple intermediate target states. The coefficients of these states are specifically selected to leverage the natural dynamics of the CR3BP and perform a passively safe inspection of the target.

Acknowledgments

C. Vela acknowledges financial support for this research by the Fulbright Foreign Student–Visiting Student Researcher program, which is sponsored by the U.S. Department of State and The Italian Ministry of Foreign Affairs.

References

[1] Luu, M., and Hastings, D. E., "Review of On-Orbit Servicing Considerations for Low-Earth Orbit Constellations," *ASCEND 2021*, AIAA Paper 2021-4207, 2021. https://doi.org/10.2514/6.2021-4207

[2] Opromolla, R., Grishko, D., Auburn, J., Bevilacqua, R., Buinhas, L., Cassady, J., Jäger, M., Jankovic, M., Rodriguez, J., Perino, M. A., et al., "Future In-Orbit Servicing Operations in the Space Traffic Management Context," *Acta Astronautica*, Vol. 220, July 2024, pp. 469–477. https://doi.org/10.1016/j.actaastro.2024.05.007

[3] Duffy, L., and Adams, J., "Cislunar Systems Architectures Survey Paper," *2022 IEEE International Systems Conference (SysCon)*, IEEE Publ., Piscataway, NJ, 2022. https://doi.org/10.1109/SysCon53536.2022.9773886

[4] Sherman, W. A., Lightsey, E. G., and Whorton, M., "Envisioning Cislunar Formation Flight: A Survey and Analysis of Enabling Mission Topologies," *ASCEND 2023*, AIAA Paper 2023-4665, 2023. https://doi.org/10.2514/6.2023-4665

[5] Guardabasso, P., Lizy-Destrez, S., and Ansart, M., "Lunar Orbital Debris Mitigation: Characterisation of the Environment and Identification of Disposal Strategies," *Proceedings of the 8th European Conference on Space Debris*, Vol. 8, European Space Agency, Paris, France, 2021.

[6] Bhatiaa, S., Shahb, K., and Kamdarc, J., "Review of Strategies for Cis-Lunar Space Traffic Management," *Proceedings of the 73rd International Astronautical Congress (IAC)*, IAF Paper IAC-22,A6, IP,80,x71015, 2022.

[7] Waldecker, C., and Howell, K., "A Design Approach for Cislunar On-Orbit Servicing Networks," *2024 AAS/AIAA Astrodynamics Specialist Conference*, AAS Paper 24-175, 2024.

[8] Waldecker, C., and Howell, K., "Satellite Servicing in Cislunar Networks with Design and Scheduling Using a Genetic Algorithm," *2025 AAS/AIAA Astrodynamics Specialist Conference*, AAS Paper 25-293, 2025.

[9] Murakami, N., Ueda, S., Ikenaga, T., Maeda, M., Yamamoto, T., and Ikeda, H., "Optimum Guidance Strategy for Rendezvous Mission in Earth-Moon L2 Halo Orbit," *Proceedings of the 25th International Symposium on Space Flight Dynamics (ISSFD)*, German Space Agency (DLR) and European Space Agency (ESA), 2015.

[10] Bando, M., Namati, H., Akiyama, Y., and Hokamoto, S., "Formation Flying Along Libration Point Orbits Using Chattering Attenuation Sliding Mode Control," *Frontiers in Space Technologies*, Vol. 3, July 2022, Paper 919932. https://doi.org/10.3389/frspt.2022.919932

[11] Corpino, S., and Stesina, F., "Inspection of the Cis-Lunar Station Using Multi-Purpose Autonomous Cubesats," *Acta Astronautica*, Vol. 175, Oct. 2020, pp. 591–605. https://doi.org/10.1016/j.actaastro.2020.05.053

[12] Bucchioni, G., and Innocenti, M., "Rendezvous in Cis-Lunar Space Near Rectilinear Halo Orbit: Dynamics and Control Issues," *Aerospace*, Vol. 8, No. 3, 2021, Paper 68. https://doi.org/10.3390/aerospace8030068

[13] Sandel, C., and Sood, R., "Natural and Forced Spacecraft Loitering in a Near Rectilinear Halo Orbit," *Journal of the Astronautical Sciences*, Vol. 71, No. 3, 2024, p. 28. https://doi.org/10.1007/s40295-024-00446-7

[14] Fu, X., and Xu, M., "Formation Flying Along Low-Energy Lunar Transfer Trajectory Using Hamiltonian-Structure-Preserving Control," *Journal of Guidance, Control, and Dynamics*, Vol. 42, No. 3, 2019, pp. 650–661. https://doi.org/10.2514/1.G003673

[15] Ceresoli, M., Zanotti, G., and Lavagna, M., "Bearing-Only Navigation for Proximity Operations on Cis-Lunar Non-Keplerian Orbits," *Proceedings of the 72nd International Astronautical Congress (IAC)*, IAF Paper IAC-21,C1,1,7,x66676, 2021.

[16] Segerman, A. M., Zedd, M. F., and Bauer, F. H., "Preliminary Planar Formation-Flight Dynamics Near Sun-Earth L2 Point," *2003 AAS/AIAA Space Flight Mechanics Meeting*, AAS Paper 03-133, 2003.

[17] Luquette, R., and Sanner, R., "Linear State-Space Representation of the Dynamics of Relative Motion, Based on Restricted Three Body Dynamics," *AIAA Guidance, Navigation, and Control Conference and Exhibit*, AIAA Paper 2004-4783, 2004. https://doi.org/10.2514/6.2004-4783

[18] Colagrossi, A., Pesce, V., Bucci, L., Colombi, F., and Lavagna, M., "Guidance, Navigation and Control for 6DOF Rendezvous in Cislunar Multi-Body Environment," *Aerospace Science and Technology*, Vol. 114, July 2021, Paper 106751. https://doi.org/10.1016/j.ast.2021.106751

[19] Colombi, F., Colagrossi, A., and Lavagna, M., "Characterisation of 6DOF Natural and Controlled Relative Dynamics in Cislunar Space," *Acta Astronautica*, Vol. 196, July 2022, pp. 369–379. https://doi.org/10.1016/j.actaastro.2021.01.017

[20] Franzini, G., and Innocenti, M., "Relative Motion Dynamics in the Restricted Three-Body Problem," *Journal of Spacecraft and Rockets*, Vol. 56, No. 5, 2019, pp. 1322–1337. https://doi.org/10.2514/1.A34390

[21] Scorsoglio, A., Furfaro, R., Linares, R., and Massari, M., "Relative Motion Guidance for Near-Rectilinear Lunar Orbits with Path Constraints via Actor-Critic Reinforcement Learning," *Advances in Space Research*, Vol. 71, No. 1, 2024, pp. 316–335. https://doi.org/10.1016/j.asr.2022.08.002

[22] Elliott, I., and Bosanac, N., "Geometric Relative Orbital Element Set for Motion Near a Periodic Orbit with Oscillatory Modes," *2020 AAS/AIAA Astrodynamics Specialist Virtual Conference*, AAS Paper 20-620, 2020.

[23] Zuehlke, D., Sizemore, A., and Henderson, T., "Periodic Relative Natural Motion in the Circular Restricted Three-Body Problem," *Proceedings of the 33rd AAS/AIAA Space Flight Mechanics Meeting*, AAS/AIAA, Austin, TX, 2023, pp. 23–112.

[24] Zuehlke, D., Tiwari, M., Jebari, K., and Kidambi, K. B., "Rendezvous and Proximity Operations in Cislunar Space Using Linearized Dynamics for Estimation," *Aerospace*, Vol. 10, No. 8, 2023, Paper 684. https://doi.org/10.3390/aerospace10080674

[25] Bucci, L., Colagrossi, A., and Lavagna, M., "Rendezvous in Lunar Near Rectilinear Halo Orbits," *Advances in Astronautics Science and Technology*, Vol. 1, No. 1, Sept. 2018, pp. 39–43. https://doi.org/10.1007/s42423-018-0012-6

[26] Takubo, Y., Manuel, W. J., and D'Amico, S., "Passively-Safe Optimal Cislunar Relative Motion Using Local Toroidal Coordinates," *2025 AAS/AIAA Space Flight Mechanics Meeting*, AAS Paper 25-331, 2025.

[27] Brown, B. M., Eastham, M. S. P., and Schmidt, K. M., "Floquet Theory," *Periodic Differential Operators*, Springer, Berlin, 2013, pp. 1–29. https://doi.org/10.1007/978-3-0348-0528-5_1

[28] Sherrill, R. E., Sinclair, A. J., Sinha, S. C., and Lovell, T. A., "Time-Varying Transformations for Hill–Clohessy–Wiltshire Solutions in Elliptic Orbits," *Celestial Mechanics and Dynamical Astronomy*, Vol. 119, No. 1, May 2014, pp. 55–73. https://doi.org/10.1007/s10569-014-9543-x

[29] Sherrill, R. E., Sinclair, A. J., Sinha, S. C., and Lovell, T. A., "Lyapunov-Floquet Control of Satellite Relative Motion in Elliptic Orbits," *IEEE Transactions on Aerospace and Electronic Systems*, Vol. 51, No. 4, 2015, pp. 2800–2810. https://doi.org/10.1109/TAES.2015.140281

[30] Ogundele, A. D., Agboola, O. A., and Sinha, S. C., "Application of Lyapunov–Floquet Transformation to the Nonlinear Spacecraft Relative Motion with Periodic-Coefficients," *Acta Astronautica*, Vol. 187, Oct. 2021, pp. 24–35. https://doi.org/10.1016/j.actaastro.2021.06.024

[31] Scheeres, D. J., Hsiao, F.-Y., and Vinh, N. X., "Stabilizing Motion Relative to an Unstable Orbit: Applications to Spacecraft Formation Flight," *Journal of Guidance, Control, and Dynamics*, Vol. 26, No. 1, 2003, pp. 62–73. https://doi.org/10.2514/2.5015

[32] Burnett, E. R., and Schaub, H., "Modal Decomposition of Spacecraft Relative Motion in Quasi-Periodic Orbits," *2020 AAS/AIAA Astrodynamics Specialist Virtual Conference*, AAS Paper 20-506, 2020.

[33] Burnett, E. R., and Schaub, H., "Geometric Perspectives on Fundamental Solutions in the Linearized Satellite Relative Motion Problem," *Acta Astronautica*, Vol. 190, Jan. 2022, pp. 48–61. https://doi.org/10.1016/j.actaastro.2021.09.028

[34] Burnett, E. R., and Schaub, H., "Spacecraft Relative Motion Dynamics and Control Using Fundamental Modal Solution Constants," *Journal of Guidance, Control, and Dynamics*, Vol. 45, No. 10, 2022, pp. 1786–1799. https://doi.org/10.2514/1.G006603

[35] Bai, X., Huang, M., Xu, M., and Liu, J., "Reconfiguration Optimization of Relative Motion Between Elliptical Orbits Using Lyapunov-Floquet Transformation," *IEEE Transactions on Aerospace and Electronic Systems*, Vol. 59, No. 2, 2022, pp. 923–936. https://doi.org/10.1109/TAES.2022.3193089

[36] Cuevas del Valle, S., Urrutxua, H., and Solano-López, P., "Optimal Floquet Stationkeeping Under the Relative Dynamics of the Three-Body Problem," *Aerospace*, Vol. 10, No. 5, 2023, p. 393. https://doi.org/10.3390/aerospace10050393

[37] Albert, S. W., and Schaub, H., "Relative Motion in the Velocity Frame for Atmospheric Entry Trajectories," *Journal of Spacecraft and Rockets*, Vol. 60, No. 5, 2023, pp. 1614–1624. https://doi.org/10.2514/1.A35753

[38] Guffanti, T., and D'Amico, S., "Integration Constants as State Variables for Optimal Path Planning," *2018 European Control Conference (ECC)*, IEEE Publ., Piscataway, NJ, 2018, pp. 3197–3202. https://doi.org/10.23919/ECC.2018.8550448

S. Chung
Associate Editor